Winter 12-15-2019

Development of High-speed Photoacoustic Imaging technology and Its Applications in Biomedical Research

Yun He
Washington University in St. Louis

WASHINGTON UNIVERSITY IN ST. LOUIS

School of Engineering and Applied Science
Department of Biomedical Engineering

Dissertation Examination Committee:
Lihong V. Wang, Co-Chair
Quing Zhu, Co-Chair
Mark A. Anastasio
Hong Chen
Jin-Moo Lee
Jung-Tsung Shen

Development of High-speed Photoacoustic Imaging technology and Its Applications in Biomedical Research

by
Yun He

A dissertation presented to
The Graduate School
of Washington University in
partial fulfillment of the
requirements for the degree
of Doctor of Philosophy

December 2019
St. Louis, Missouri

Table of Contents

List of Figures

List of Tables

Acknowledgments

First, I thank my supervisor Prof Lihong V. Wang, for his support and funding throughout my dissertation work. It is a great journey working in his lab, conducting mind-blowing researches, and gaining my independence. The lab members he put together are the best help I can get for my researches. I would like to express my sincere gratitude to my colleagues for their generous help and inspirations, including Lidai Wang, Junjie Yao, Junhui Shi, Ruiying Zhang, Terence Wong, Hsun-Chia Hsu, Yang Li, Toru Imai and Konstantin Maslov. It is a great honor learning from these leading people in the field.

I also give my thanks to my collaborators Drs Chih-Hsien Huang, Jun Zou, Ruimin Chen, and Qifa Zhou. Their respective expertise is extremely critical for moving my dissertation forward.

Next, I thank my committee members, Profs Quing Zhu, Jin-Moo Lee, Jung-Tsung Shen, Hong Chen, and Mark Anastasio. I appreciate their valuable advice and supports.

I can never thank enough for the patience Prof Jim Ballard had while meticulously editing my manuscripts. He did not want me to use the word “meticulous” when acknowledging him in my papers, so I formally state my appreciation here in my own words.

Last, I give my greatest love to my families. It is their unconditional supports that carried me through all these years of extremely hard working. I would not succeed in finishing this dissertation without their love.

Yun He

Washington University in St. Louis

December 2019

Dedicated to my families.

ABSTRACT OF THE DISSERTATION

Development of High-speed Photoacoustic Imaging technology and Its Applications in Biomedical Research

by

Yun He

Doctor of Philosophy in Biomedical Engineering

Washington University in St. Louis, 2019

Professor Lihong V. Wang, Co-Chair

Professor Quing Zhu, Co-Chair

Photoacoustic (PA) tomography (PAT) is a novel imaging modality that combines the fine lateral resolution from optical imaging and the deep penetration from ultrasonic imaging, and provides rich optical-absorption–based images. PAT has been widely used in extracting structural and functional information from both *ex vivo* tissue samples to *in vivo* animals and humans with different length scales by imaging various endogenous and exogenous contrasts at the ultraviolet to infrared spectrum. For example, hemoglobin in red blood cells is of particular interest in PAT since it is one of the dominant absorbers in tissue at the visible wavelength.

The main focus of this dissertation is to develop high-speed PA microscopy (PAM) technologies. Novel optical scanning, ultrasonic detection, and laser source techniques are introduced in this dissertation to advance the performance of PAM systems. These upgrades open up new avenues for PAM to be applicable to address important biomedical challenges and enable fundamental physiological studies.

First, we investigated the feasibility of applying high-speed PAM to the detection and imaging of circulating tumor cells (CTCs) in melanoma models, which can provide valuable information

about a tumor's metastasis potentials. We probed the melanoma CTCs at the near-infrared wavelength of 1064 nm, where the melanosomes absorb more strongly than hemoglobin. Our high-speed PA flow cytography system successfully imaged melanoma CTCs in travelling trunk vessels. We also developed a concurrent laser therapy device, hardware-triggered by the CTC signal, to photothermally lyse the CTC on the spot in an effort to inhibit metastasis.

Next, we addressed the detection sensitivity issue in the previous study. We employed the stimulated Raman scattering (SRS) effect to construct a high-repetition-rate Raman laser at 658 nm, where the contrast between a melanoma CTC and the blood background is near the highest. Our upgraded PA flow cytography successfully captured sequential images of CTCs in mouse melanoma xenograft model, with a significantly improved contrast-to-noise ratio compared to our previous results. This technology is readily translatable to the clinics to extract the information of a tumor's metastasis risks.

We extended the Raman laser technology to the field of brain functional studies. We developed a MEMS (micro-electromechanical systems) scanner for fast optical scanning, and incorporated it to a dual-wavelength functional PAM (fPAM) for high-speed imaging of cerebral hemodynamics in mouse. This fPAM system successfully imaged transient changes in blood oxygenation at cerebral micro-vessels in response to brief somatic stimulations. This fPAM technology is a powerful tool for neurological studies.

Finally, we explored some approaches of reducing the size the PAM imaging head in an effort to translate our work to the field of wearable biometric monitors. To miniaturize the ultrasonic detection device, we fabricated a thin-film optically transparent piezoelectric detector for detecting PA waves. This technology could enable longitudinal studies on free-moving animals through a wearable version of PAM.

Chapter 1: Introduction

This chapter introduces the concept, implementation, and applications of photoacoustic tomography (PAT). In section 1.1, the physical mechanism of PAT is reviewed, followed by an introduction to several representative implementations of PAT. In section 1.2, an outline of this dissertation is given.

1.1 Introduction to Photoacoustic Tomography

PAT is an imaging technology based on the photoacoustic (PA) effect[1], in which the short-pulsed laser energy absorbed by biomolecules is first converted to heat through non-radiative relaxation[2]. Subsequently, the spatially confined heat is converted to a pressure rise via thermoelastic expansion, and the initial pressure rise propagates in tissue as an ultrasonic wave—PA wave[2]. This PA wave is usually detected by one or a matrix of ultrasonic transducers to reconstruct the mapping of the optical absorption in tissue[3]. PAT is also a highly scalable imaging modality, capable of imaging objects of a broad range of length scales, from organelles to organs, with respective appropriate resolutions[4].

Photoacoustic microscopy (PAM) is the microscopic implementation of PAT[5]. In a standard PAM setup, a pulsed laser beam is focused onto the tissue. And a high-frequency ultrasonic transducer is placed co-axially with the laser beam to detect the PA waves with high sensitivity[6]. The acquired PA signal, A-line, is temporally resolved to form a one-dimensional (1D) image along the axial direction (depth-resolved image). A three-dimensional (3D) image is acquired by raster scanning (C-scan) the probing laser or the imaging object[7, 8].

1.2 Dissertation outline

This dissertation is focused on the development and applications of PAM. It is arranged in the following structure.

Chapter 2 describes the development of a PAM technology for high-speed flow cytography of circulating melanoma cells in vivo, which exploits the high optical absorption contrast between melanoma cells and the blood background. We also developed a concurrent on-demand laser therapy device that works in a selective identify-then-locally-administer manner, in an effort to inhibit cancer metastasis.

Based on the previous work, Chapter 3 addresses some technological limitations of Chapter 2 by improving the detection sensitivity of PAM. We explore a wavelength conversion technique, stimulated Raman scattering, to probe the circulating melanoma cells at a laser wavelength that gives higher contrast. It achieves a detection sensitivity at least 4 times higher than that in Chapter 2, and successfully imaged circulating melanoma cells in a tumor xenograft model.

Chapter 4 extends the work in Chapter 3. It introduces a dual-wavelength high-speed function PAM (fPAM) based on a Raman laser. Both the scanning and detection devices are significantly improved with novel techniques. We applied this fPAM in studies of mouse brain activity in response to somatic stimulations, and resolved transient hemodynamic changes on a single micro-vessel scale.

Chapter 5 extends the scope of Chapter 4. It explores some approaches towards wearable PAM. A lithium niobate-based optically transparent ultrasonic transducer is developed to minimize the ultrasonic detection device. Its application in PAM is demonstrated with a phantom and small animal experiment.

Chapter 6 summarizes all the works in this dissertation, and outlines some prospective studies for each chapter.

Chapter 2: *In vivo* label-free photoacoustic flow cytography and on-the-spot laser killing of single circulating melanoma cell

This chapter introduces a hybrid PAM and laser therapy system for the application of flow cytography and destruction of circulating tumor cells (CTCs). Here we focused on the skin cancer melanoma. Exploiting the exquisite intrinsic optical absorption contrast of melanoma CTCs in the blood background, we developed dual-wavelength photoacoustic flow cytography coupled with a nanosecond-pulsed melanoma-specific laser therapy device. We have successfully achieved *in vivo* label-free imaging of rare single circulating melanoma cells in both arteries and veins of mice. Further, the photoacoustic signal from a circulating melanoma cell immediately hardware-triggers a lethal pinpoint laser irradiation to kill it on the spot in a thermally confined manner without collateral damage. A pseudo-therapy study including both *in vivo* and *in vitro* experiments demonstrated the performance and the potential clinical application of our technology, which can facilitate early treatment of metastasis in a dialysis manner by clearing circulating tumor cells from vasculature. The work in this chapter has been published in *Scientific Reports*[9].

2.1 Background

As many as 90% of cancer-related deaths are attributed to metastases, the process of cancer cells spreading from a primary site to surrounding and distant sites to form new tumor colonies[10-13]. Most metastasis cases take the route of hematogenous dissemination of CTCs, including steps such as a tumor cell with invasive phenotypes intravasating local blood vessels, surviving in blood circulation, extravasating the vessel wall[14]. Here we focused on the deadliest type of skin cancer, melanoma. In United States, it has more than 87,000 new diagnoses and 10,000 deaths each year[15]. Melanoma has a high tendency to metastasize even at an early stage, after which the 5-year survival

rate decreases from 98.5% to less than 20%[15]. The presence and concentration of CTCs are closely correlated with tumor progression, metastases, and survival rates in patients[16]. Therefore, efficient detection and early eradication of melanoma CTCs are vital for cancer diagnosis and improving patient prognosis.

Clinical *ex vivo* CTC detection with high sensitivity remains a challenge since it heavily depends on both small-volume sampling of blood and labeling of biomarkers on the cell membrane[17, 18]. Extensive *in vivo* CTC detection studies employing fluorescence probes or multiplex nanoparticles have achieved promising results[17, 19-21], but the biosafety and labeling efficiency remain critical concerns, which limits their clinical translation. In the biological tissue background, melanoma cells have a high melanosome expression, providing a striking endogenous absorption contrast in the red to near-infrared (NIR) spectrum[22, 23]. Hence, PAT, having the highest possible sensitivity to absorption contrast, is an excellent technology for label-free imaging of melanoma cells. In 2009, Galanzha et al. reported label-free detection of melanoma CTCs *in vivo* using PA cytometry, in which a pulsed laser was focused across a blood vessel and an ultrasonic transducer collected PA signals from a large voxel[24]. This design enables detection of melanoma CTCs in situ, but it lacks imaging capabilities. A recently developed optical-resolution PA imaging technique has acquired images of single CTCs *in vivo*[25]. However, its non-optic-acoustic-confocal configuration and low CTC-to-background contrast limit the applications to capillaries and require complicated pattern recognition to identify CTCs. High-contrast flow cytography that can reliably distinguish CTCs in real-time is needed for on-the-fly targeted CTC therapies.

Traditional clinical therapies for tumor metastasis are still palliative, with many drugs not reaching metastasis sites[26]. Novel therapies based on particular metastasis features, such as angiogenesis, lymphangiogenesis, specific signal pathways and biomarkers, have reported good clinical

outcome[26, 27], but they have less efficacy on initial micro-metastasis sites and typically produce adverse side effects[28, 29]. Taking another approach, therapies directly targeting CTCs can reduce tumor metastasis potentials and may even prevent metastasis from occurring if administered in early tumor stages[13]. Nanosecond-pulsed lasers at 680–1064 nm wavelengths have long enabled physicians to treat melanocytic skin lesions with a high degree of selectivity and a low risk of postoperative complications[30, 31]. For laser pulses shorter than the thermal relaxation time, radiant energy is largely confined in the absorber, which can achieve efficient energy delivery and selective photothermolysis of the absorbing cells[32]. When a nanosecond laser pulse with sufficient energy irradiates a melanoma CTC, the melanosomes inside are heated beyond the threshold temperature for explosive vaporization, photomechanically killing the CTC without damaging any adjacent tissue components[32, 33].

Here we report high-resolution CTC imaging, using our new dual-wavelength PA flow cytography technology, in combination with real-time CTC destruction at the single-cell scale by pinpoint nanosecond-pulsed lethal irradiation from a therapy laser. We obtained images of single CTCs flowing in both arteries and veins on the fly, and performed real-time CTC destruction in vivo in small animals. The performance of this system was demonstrated by a study mimicking treatment of melanoma metastasis.

2.2 Methods

2.2.1 Dual-wavelength PA flow cytography

To induce PA signals, we employed a high-repetition-rate picosecond laser (APL-4000-1064, Attodyne, Inc.; maximum pulse repetition rate: 500 kHz) to provide 6-ps laser pulses at 1064 nm and 532 nm wavelengths. After traveling a 25-meter delay line, the 532 nm laser beam was combined with the 1064 nm laser beam through a longpass dichroic mirror. Melanosome absorbs

similarly to Hb at 532 nm, but >10 times more strongly than Hb at 1064 nm, which provides a high CTC contrast against the RBC background. The combined laser beams were focused by a focusing lens, reflected by an optical-acoustic combiner (OAC), and directed to the target by a water-immersible MEMS (micro-electro-mechanical system) scanner for 1D fast scanning. The target was mounted on a stepper-motor-driven translational stage to facilitate orthogonal slow axis scanning. The OAC comprised of an aluminum-coated prism and an uncoated prism, and the thin aluminum coating on the first prism reflected light but transmitted sound. A correction lens was attached to the top surface of the OAC to correct the optical aberration due to the prisms. Excited PA waves were also reflected by this MEMS mirror, collected by an acoustic lens, transmitted through the OAC, and detected by an ultrasonic transducer (V214-BB-RM, Olympus-NDT, Inc.). Since the 532 nm laser pulse traveled through the ~80-ns delay line, the PA wave induced by the 532 nm laser pulse arrived ~80 ns later than that by the 1064 nm laser pulse (Figure 2.1a). PA signals were then amplified by two radio-frequency amplifiers (ZX60-3018G-S+ and ZFL-500LN+, Mini-circuits, Inc.) and acquired by a high-speed digitizer (ATS9350, Alazar Tech, Inc.). By steering both the optical and acoustic axes simultaneously, the system maintained confocal alignment over the entire FOV, providing high detection sensitivity. This flow cytography was capable of volumetric (3D) imaging at 10 Hz over a FOV of 3 × 0.25 mm^2 at a depth up to ~0.7 mm, with a 3 μm lateral resolution for the 532 nm flow cytography images, 7 μm for the 1064 nm flow cytography images, and ~26 μm axial (depth) resolution for both. The length and width of the FOV can be tuned by varying the driving voltage of the MEMS mirror and by adjusting the scanning range of the stepper motor, respectively. It is also possible to achieve a higher frame rate at the expense of a larger scanning step size, as in Figure 2.3, or of a shorter range for the stepper motor.

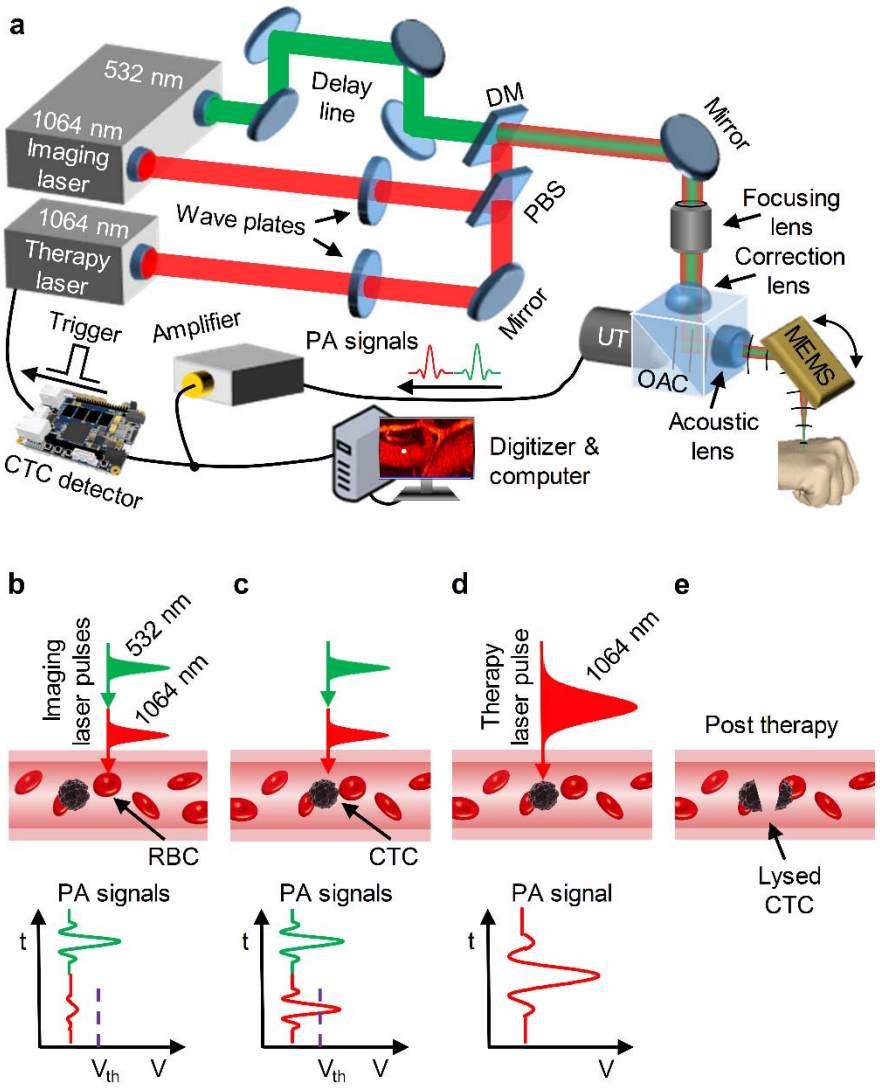

Figure 2.1 CTC imaging and destruction by dual-wavelength PA flow cytography combined with laser therapy. (**a**) Schematic of selected components of the experimental system. DM, dichroic mirror; MEMS, micro-electro-mechanical-system scanning mirror; OAC, optical-acoustic combiner; PBS, polarizing beamsplitter; UT, ultrasonic transducer. The 1064 nm and 532 nm imaging lasers are employed to image CTCs and vasculature, respectively. (**b-e**) Scheme of real-time detection and laser killing of CTCs. The CTC detector compares the earlier 1064 nm laser-induced CTC-specific PA signal against an optimized threshold level (purple dashed line in (**b**) and (**c**)) above the Hb signal, and thus can reliably distinguish CTCs and trigger the therapy laser (**c**). Within ~10 μs, the therapy laser is fired and focused to the detected CTC location to photomechanically kill the CTC (**e**).

2.2.2 On-the-fly CTC detection

PA signals were concurrently analyzed for melanoma CTC detection based on the melanosome-specific 1064 nm absorption induced PA signals (Figure 2.2). The specially built CTC detector consisted of an ultrafast analog switch and a comparator (Figure 2.2). Based on the fixed 80-ns

time interval between the 1064 nm and 532 nm laser pulses, a time window signal controlled the analog switch as a gate to selectively transmit the earlier 1064 nm laser-induced PA signal. The comparator compared this gated PA signal with an optimized preset threshold voltage. A signal above the threshold indicated the presence of a melanoma CTC, and immediately triggered a high-pulse-energy therapy laser (INNOSLAB, EdgeWave, Inc.) to lethally irradiate the same CTC on the spot (Figure 2.1c-d). Following a successful CTC detection, the detector was disabled for 1 ms to prevent double triggering by the much-higher-amplitude therapy laser-induced PA signal.

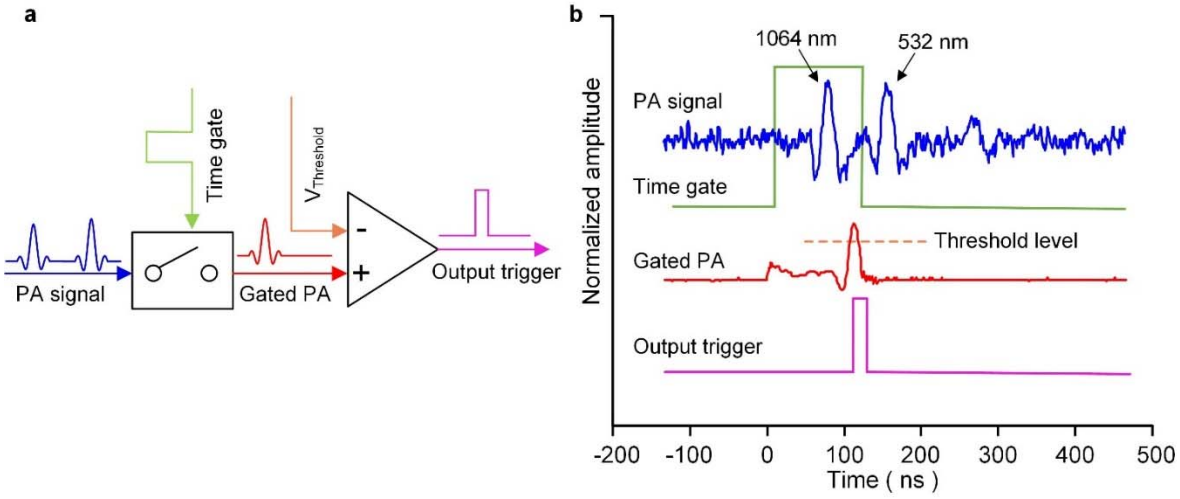

Figure 2.2 Circuit diagram and performance of the lab-made CTC detector. (**a**) Circuit diagram. The time gate signal (TTL logic) controls an ultrafast analog switch (SN74LVC1G3157, Texas Instruments Inc.) as a gate. Based on the fixed 80-ns time interval between the 1064 nm and 532 nm laser pulses in the dual-wavelength flow cytography, the time gate signal is employed to selectively gate the PA signals, allowing only the earlier PA signal induced by the 1064 nm laser pulse to pass through to the comparator. The voltage comparator (TLV3502, Texas Instruments Inc.; 4.5 ns propagation time) compares the gated PA signal to distinguish CTCs from RBCs and other blood cells. Once the signal peak is above the optimized preset threshold voltage (80 mV), a trigger signal is generated for the therapy laser. The high-speed characteristics of the analog switch and comparator guarantee real-time CTC detection and therapy-laser triggering. (**b**) Time sequence plot of the PA signal, time gate control signal, gated PA signal, and output trigger. The time interval from the 1064 nm laser-induced PA signal from a CTC to the output trigger is ~30 ns.

2.2.3 Real-time CTC destruction

Melanoma CTCs were irradiated by a high-pulse-energy 1064 nm laser pulse (7 ns) that could mechanically destroy the CTCs by explosive vaporization of the melanosomes inside (Figure

2.1de)[32-34]. The thermal diffusion distance during 7-ns laser exposure is ~30 nm, which means the thermal damage is confined to melanosomes, ~500 nm in diameter[32]. The therapy laser beam was coaxially aligned with the imaging laser beams by a polarizing beamsplitter and focused onto the CTC location. In order to maximize combining efficiency, a half-wave plate was used to adjust the polarization of the therapy laser beam. We optimized the focal spot size of the therapy laser based on the scanning speed of the MEMS mirror, the signal propagation and processing time, the CTC flow speed, and the therapy laser's trigger-to-emission delay. The maximum scanning speed of the laser focal spot on the target was ~1 m/s. The acoustic flight time from the absorber to the ultrasonic transducer was ~10 μs, while the signal processing time in the CTC detector circuits was ~30 ns and the trigger-delay time of the therapy laser was ~300 ns. Based on the blood flow speed, the CTC movement in blood vessel during the ~10 μs response time was negligible. In conclusion, the center of the therapy laser's focal spot could be ~10 μm (1 m/s × 10 μs) away from the original imaged CTC location. Therefore, the focal spot of the therapy laser, with 25 J/cm^2 fluence, was adjusted to be 50 μm in diameter to ensure coverage of the entire CTC with a sufficient local radiant intensity.

2.2.4 Experimental animals

Adult female ND4 Swiss Webster mice (Hsd: ND4, Envigo, Inc.; 20-25 g, 10-12 weeks old) were used for the *in vivo* CTC imaging and laser killing experiment. The laboratory animal protocols were approved by the Animal Studies Committee of Washington University in St. Louis. Three days before the experiment, cannulation was performed to safely insert a catheter into the jugular vein or carotid artery of the mouse, and the hair on the mouse ear was removed with human hair-removing lotion. During the experiment, the mouse was maintained under anesthesia with 1.5% vaporized isoflurane, and taped to a lab-made animal holder, which was mounted on the stepper-

motor-driven translation stage. Ultrasound gel was then applied to the imaging area to retain moisture and couple acoustic signals. A water tank filled with deionized water was then placed on top of the mouse ear. The membrane at the bottom of the water tank was in gentle contact with the ultrasound gel. During imaging, a 0.1-ml suspension containing ~10^6 B16F10 melanoma cells was injected through the cannulation catheter. The cells were cultured in DMEM supplemented with 10% fetal bovine serum at 37 ºC in a humidified atmosphere with 5% CO_2.

Female athymic nude mice (Hsd:Athymic Nude-Foxn1, Envigo, Inc.; 12-15 g, 3-4 weeks old) were used for the pseudo-therapy study. The laboratory animal protocols were approved by the Animal Studies Committee of Washington University in St. Louis. Before the study, the mice were randomly assigned into either the therapy group or the control group. In one experiment, a mixture was first prepared by diffusing cultured B16F10 melanoma cells into bovine blood (Defibrinated Bovine Blood, Quad Five, Inc.). Next, this mixture was pumped in a translucent silicone tube (300 μm inner diameter and 640 μm outer diameter)—mimicking a blood vessel—through our system with the therapy laser turned on. The flow rate was set at ~80μL/hr, with ~20 CTCs passing through the system every second. Afterwards, the cell mixture was reduced in volume by centrifugation to make a 50 μL dose (containing ~10^5 cells) that was subcutaneously inoculated into the dorsal area of a nude mouse in the therapy group. Then, another vial of mixture was acquired in a similar manner but with the therapy laser turned off, and a 50 μL dose of this imaged (but not treated) mixture was inoculated into a nude mouse in the control group. Afterwards, all the mice were imaged by acoustic resolution PAM to detect tumor formation and to measure the volume of flat tumors, and raised tumors were measured using a caliper[35]. Mice were euthanized when the tumor dimension exceeded 2 cm or the tumor began to ulcerate.

2.3 Results

2.3.1 Imaging results

To exploit the NIR absorption contrast between melanosome and hemoglobin (Hb) in red blood cells (RBCs), and to image CTCs on the fly, we developed a fast scanning PA flow cytography system for high-speed imaging at both 532 nm and 1064 nm wavelengths with single-cell resolution coupled with real-time selective CTC destruction by nanosecond-pulsed NIR laser-induced photothermolysis (Figure 2.1). The therapy laser beam is coaxially aligned with the two imaging laser beams, and is triggered, using real-time hardware, immediately after flow cytography detects a CTC (Figure 2.1b-e, Figure 2.2). We first validated the system's ability to image single CTCs with the therapy laser turned off. To simulate CTCs, ~10^6 cultured B16F10 melanoma cells were administrated into the mouse's blood circulation system through jugular vein cannulation, and a portion of these cells survived in circulation as CTCs. A 1.2 × 0.3 mm^2 area of an artery-vein pair in the mouse ear was imaged by flow cytography at a 16.6 Hz volumetric (3D) rate. Figure 2.3 shows some snapshots of single CTCs flowing through the field of view (FOV) in the artery and the vein. As shown in Figure 2.3a, the vascular structure was imaged with high contrast by the 532 nm laser owing to the strong light absorption by Hb in RBCs at this wavelength. However, CTCs can hardly be distinguished from RBCs in these images, mainly due to the similar absorption coefficients for melanosome and Hb at 532 nm. In comparison, the 1064 nm laser pulse excitation of a CTC produced a PA signal with ~5 times greater amplitude than the background, while RBC signals were below the noise level. We performed control studies for 20 minutes before cell injection and recorded no PA signals of a similar amplitude level, which verified that the high-amplitude 1064 nm laser-induced PA signals indeed originated only from CTC absorption. The

arterial and venous flow speeds of the CTC were calculated to be 0.33 mm/s and 0.20 mm/s, respectively, which are in general accordance with previously reported values.

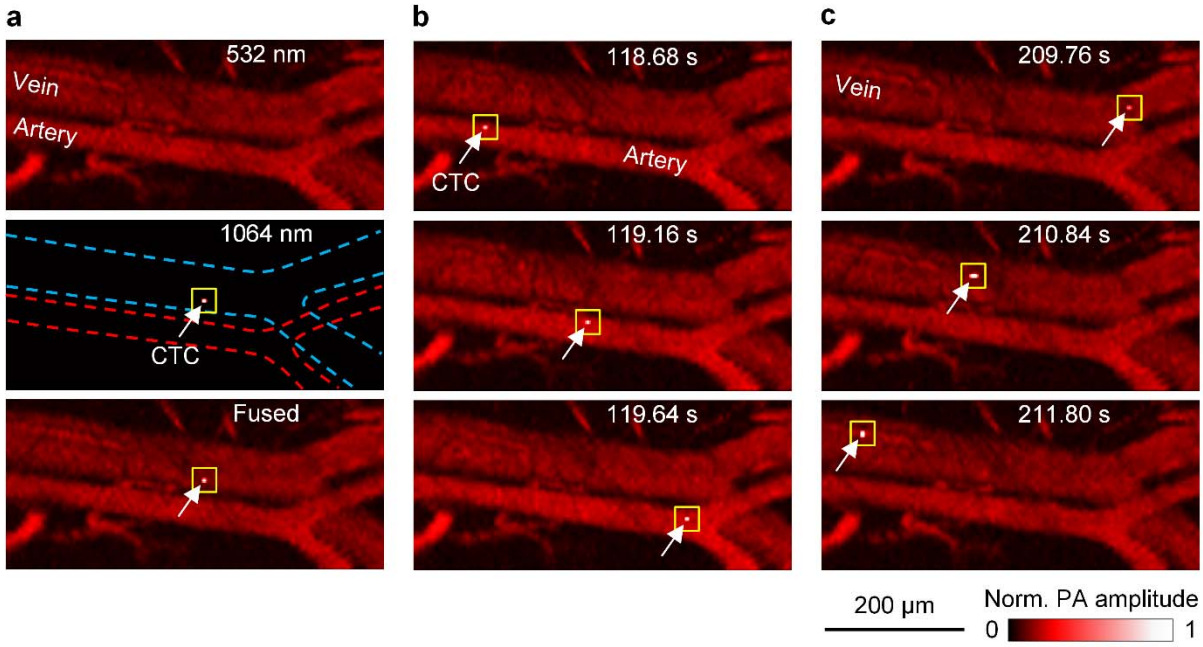

Figure 2.3 Snapshots showing single CTCs travelling in vasculature. (**a**) 532 nm laser-induced (Top), 1064 nm laser-induced (Middle), and fused (Bottom) flow cytography images. In the 1064 nm laser-induced image, the white arrow and yellow square indicate the detected CTC; the red and blue dashed lines delineate the artery and vein boundaries, respectively. (**b**) Three fused snapshots spanning ~1 s, showing a single CTC traveling in the artery. (**c**) Three fused snapshots spanning ~2 s, showing a single CTC traveling in the vein. The times labeled in (**b**) and (**c**) are relative to CTC injection.

A CTC cluster flowing in an artery was also imaged *in vivo* in a carotid artery cell injection experiment (Figure 2.4). No return of this CTC cluster was observed, which indicated that it might have been clogged at a vascular branching point, seeding a secondary tumor.

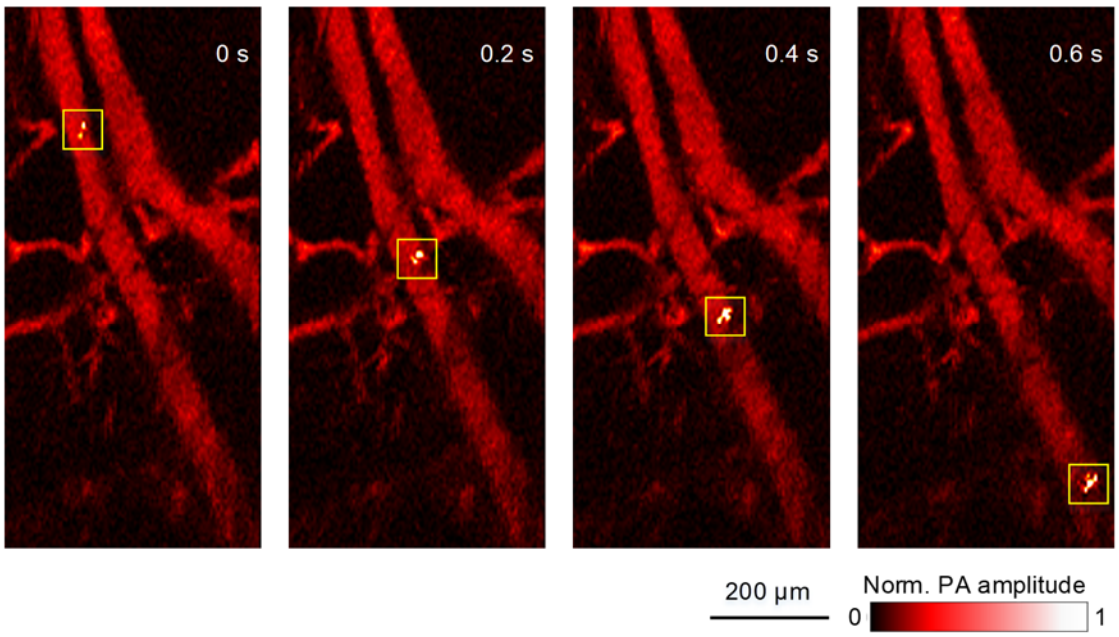

Figure 2.4 Sequential flow cytography images of a CTC cluster flowing through an artery in a mouse ear. About 10^6 cultured B16F10 cells were administered through carotid artery cannulation. Some of the cells were naturally bound together by cell adhesion as clusters. A 2.0 × 0.5 mm^2 area of vasculature over a depth of ~150 µm in the mouse ear was imaged by flow cytography at a 5 Hz volumetric (3D) rate. As it flowed through the FOV, a CTC cluster in the artery was imaged in four successive frames. The size of the cluster was estimated to be 25-40 µm. Since the dynamics of CTC clusters may be turbulent inside the blood vessel and the scanning step size is ~5 µm, the PA signal of the CTC cluster fluctuated.

2.3.2 Therapy results

To investigate the radiant energy required to kill a CTC, we used a single-shot 1064 nm laser pulse to irradiate cultured B16F10 melanoma cells *in vitro*. Different areas of a monolayer of melanoma cells were irradiated with increasing levels of laser fluence, and then the cells were stained with trypan blue to test cell viability (Figure 2.5). The results indicated that a 1064 nm laser pulse with 8.8 J/cm^2 fluence was sufficient to guarantee cell death.

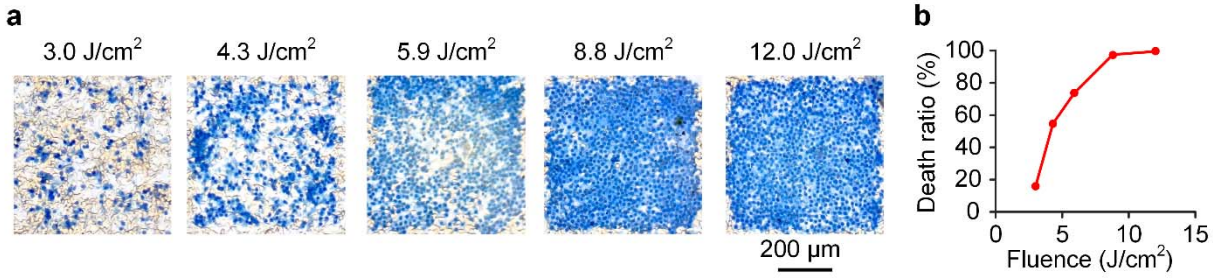

Figure 2.5 Irradiation of melanoma cells in vitro. (**a**) B16 cells on glass slides were irradiated by increasing levels of laser fluence and stained with trypan blue to test cell viability. (**b**) Plot of cell death percentage versus laser fluence.

Potential tissue damage by the therapy laser was also carefully investigated. A monolayer of RBCs was imaged by phase contrast microscopy before and after 30 J/cm^2 laser irradiation (Figure 2.6). Comparison of the two images indicated no apparent change, with both showing donut-shaped morphology.

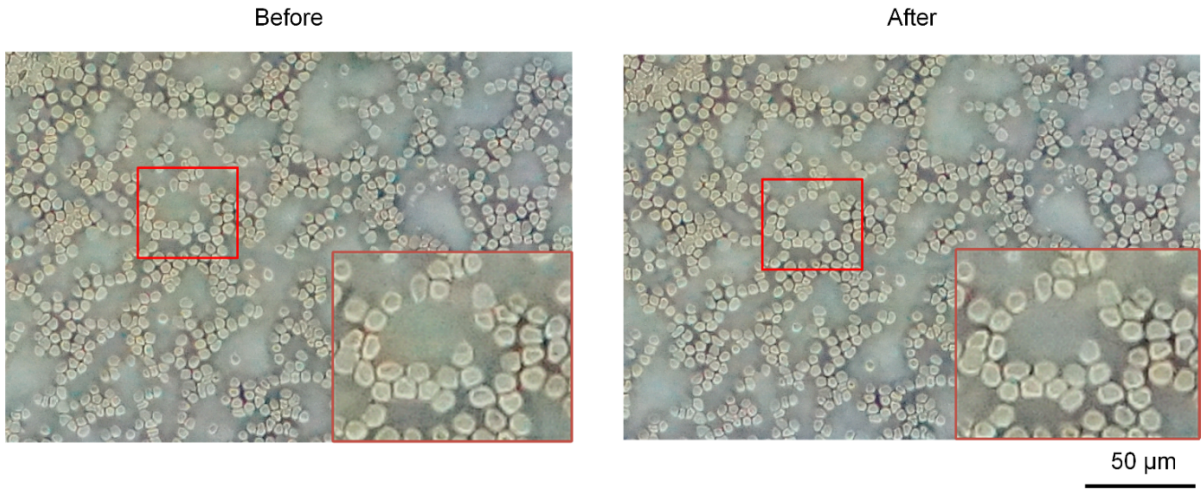

Figure 2.6 Phase-contrast images of RBCs acquired before and after exposure to single-shot 1064 nm laser irradiation with 30 J/cm^2 fluence. Close-ups of the same region (enclosed by the red rectangles) before and after exposure, placed at the bottom right corners of the two images, indicate no apparent morphological change.

In addition, measuring the optical absorbance of the supernatant showed no RBC hemolysis in blood samples exposed to 30 J/cm^2 laser irradiation (Figure 2.7).

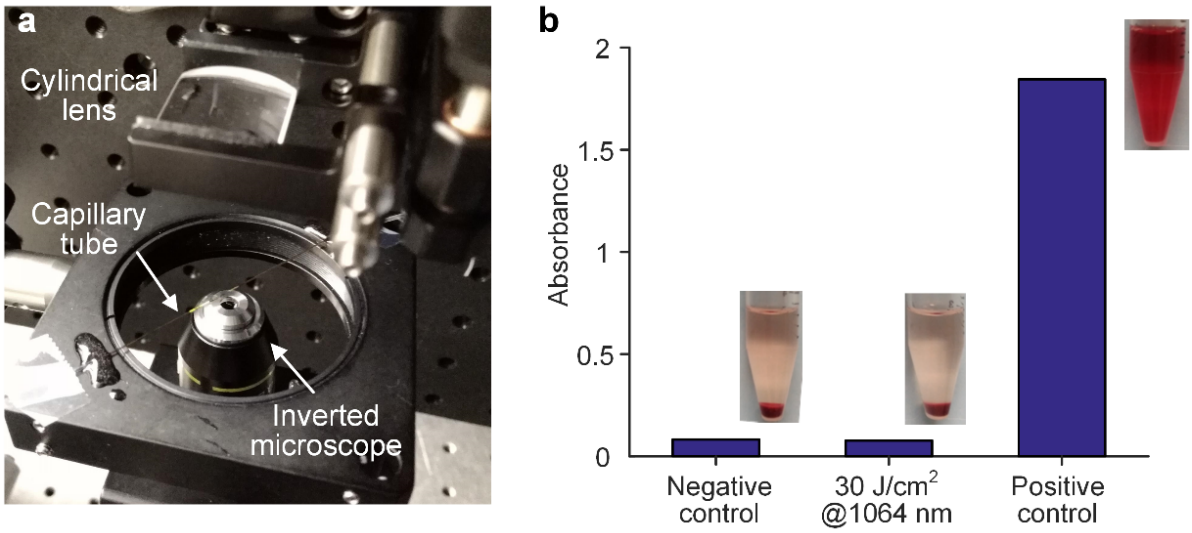

Figure 2.7 RBC hemolysis study results. (**a**) Potential RBC hemolysis by an energetic 1064 nm laser was studied by irradiating flowing blood samples at a 30 J/cm^2 fluence level. Bovine blood was washed three times with saline before the experiment, then it was pumped through a glass tube (100 µm inner diameter) at a 0.15 mm/s flow speed. Laser light (5 kHz repetition rate) was focused across the tube by a cylindrical lens with a 30 µm focal width. An inverted microscope was used to help position the tube in the focal zone of the lens. (**b**) The optical absorbance of the supernatants at 532 nm indicates no detectable hemolysis was caused by the therapy laser irradiation. For the two control groups, the therapy laser was turned off during pumping. Blood samples from the negative control and the study groups were diluted 20 times with saline, while that of the positive control group was diluted 20 times with pure water to induce total hemolysis. All blood samples are centrifuged at 3000 rpm for 10 min, and the supernatants (photos shown at the top right corner of each group) were extracted to measure their optical absorbance at 532 nm. Equation $R = (A_s - A_0)/A_{100}$ is used to calculate the hemolysis ratio R, where A_s is the absorbance of the supernatant from the study group; A_0 and A_{100} are that from blood samples with no hemolysis (negative control) and 100% hemolysis (positive control), respectively.

Therapy experiments were conducted in a similar manner to the imaging experiments. Figure 2.8 shows an event of single-CTC detection and real-time destruction. The CTC signal induced by the 1064 nm laser pulse immediately hardware-triggered a therapy laser pulse to irradiate the detected CTC with a 50 µm focal diameter and a 25 J/cm^2 fluence, above the lethal level. This lethal irradiation produced a PA signal with a much greater amplitude, ~14 times higher than the maximal imaging signal (Figure 2.8c), and its peak location indicated that the CTC was within the focal spot of the therapy laser.

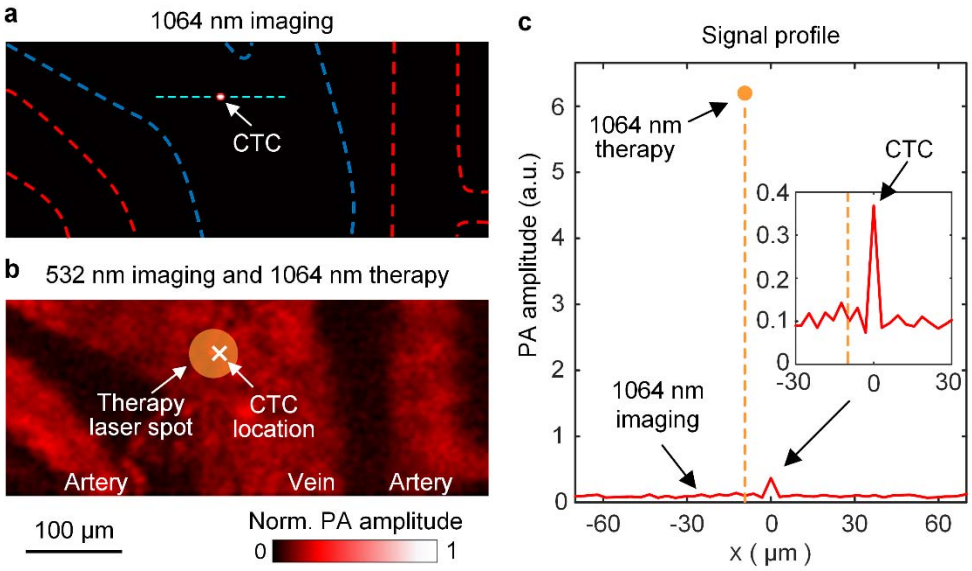

Figure 2.8 ***In vivo*** **detection and expected photothermal killing of a CTC.** The CTC was first detected in the 1064 nm laser-induced flow cytography image (**a**) and then lethally irradiated by a therapy laser pulse, also at 1064 nm, with a 50-μm focal diameter (**b**). In (**b**), The much-higher-amplitude PA signal induced by the therapy laser pulse is illustrated by the filled yellow circle. (**c**) Profile of the PA signals from the region across the CTC, indicated by the dashed cyan line in (**a**). The *x* axis, parallel with the imaging laser's scanning direction (from right to left), was centered at the CTC location. In the 1064 nm imaging laser-induced signals (red solid line), the CTC signal (shown in detail by the inset) had a contrast-to-noise-ratio (CNR) of ~25. The therapy laser-induced PA signal's peak location (dashed orange line) was only ~10 μm away from the detected CTC location, which indicated that the CTC position (white cross in (**b**)) was within the therapy laser's focal spot (circle in (**b**)).

This PA signal amplitude, measured in another experiment, was far higher than that of a regular blood vessel with the same irradiation (Figure 2.9). Therefore, we concluded that this PA signal mainly originated from light absorption by the CTC, and that this CTC was destroyed by the therapy laser irradiation. In total, four events of real-time expected photothermal killing of CTCs at different locations were recorded during 5 minutes in the experiment. Flow cytography confirmed no disturbance to blood flow during 30 min of observation after this experiment. In addition, there were no visible damages on the mouse ear.

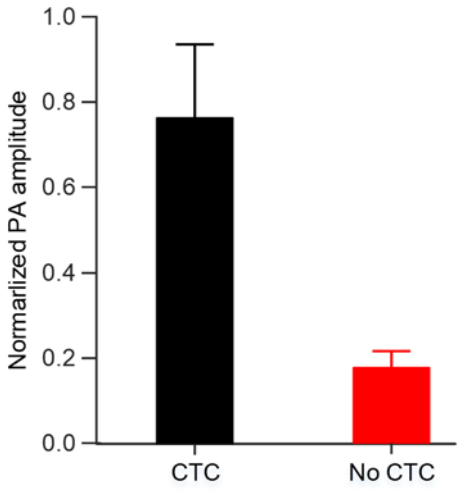

Figure 2.9 Therapy laser-induced PA signals. Therapy laser-induced PA signals from a blood vessel containing a CTC within the laser's focal spot (black), and that from the same blood vessel when it does not contain a CTC (red). Data are averaged over ten measurements; error bars show the standard deviations.

We also conducted a pseudo-therapy study to evaluate the performance of the system and demonstrate the value of this therapy scheme. Experiments were designed to mimic treating melanoma metastasis by impeding CTC dissemination (Figure 2.10a). First, cultured B16F10 cells were mixed with bovine blood and pumped into a translucent silicone tube to simulate CTCs. Then this mixture was pumped through our system to specifically detect and kill the CTCs. For the control experiment, the therapy laser was turned off during the experiment, leaving the CTCs only imaged by our system. Next, the treated and untreated mixtures were subcutaneously inoculated into two groups of nude mice, respectively, simulating hematogenous metastases.

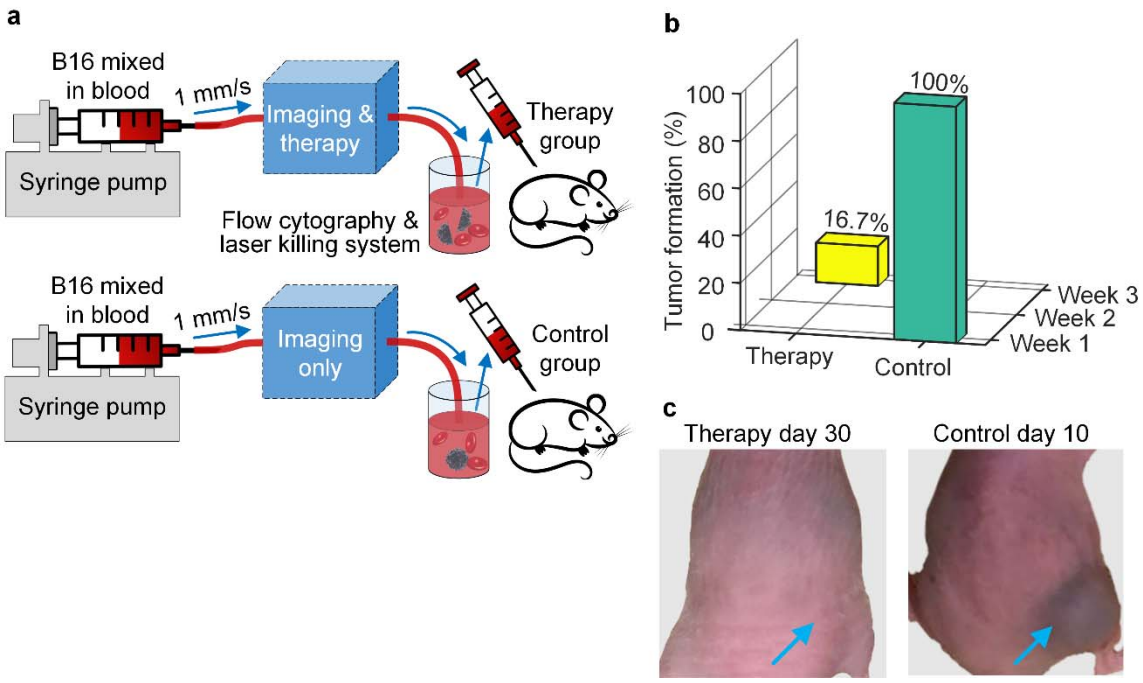

Figure 2.10 Scheme and results of the pseudo-therapy study. (**a**) The control experiment (bottom) was conducted after the therapy experiment (top) by simply switching off the therapy laser. The flow rate was set at ~80 μL/hr with ~20 CTCs flowing through the system every second. (**b**) Only 1 out of 6 therapy experiments had a tumor detected at week 3, compared to 100% tumor formation by week 1 in the control group. (**c**) Representative photos of the mice after experiments. (Left) No tumor was detected around the inoculation site (blue arrow) in 30 days following a therapy experiment. (Right) A raised tumor (blue arrow) was observed 10 days after a control experiment.

Afterwards, the area around each inoculation site was imaged every week by acoustic resolution (AR) PAM[36, 37] at 750 nm wavelength, to monitor tumor formation (Figure 2.11).

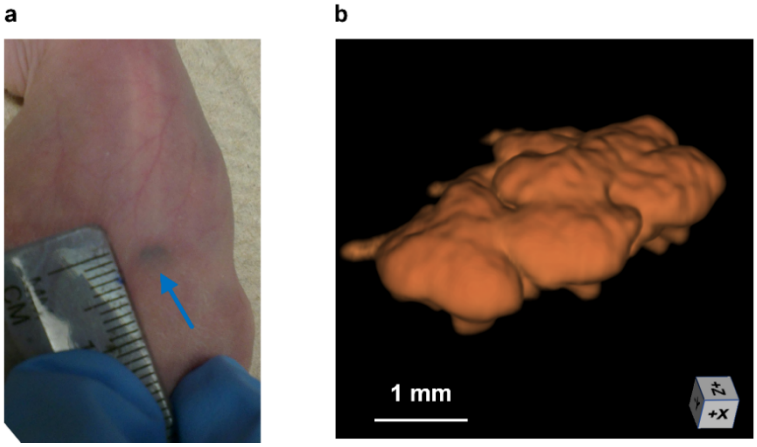

Figure 2.11 Tumor size measurement. (**a**) Photograph of a flat tumor (blue arrow) in the control group taken 5 days after experiment. (**b**) Three-dimensional AR-PAM image of this tumor. Its volume is calculated to be 2.01 mm^3.

After 30 days, only one of the six therapy experiments resulted in a tumor formation, and that tumor had a significantly slower growth, in comparison to the rapid tumor formation and growth following every control experiment (Figure 2.10bc, Figure 2.12). This only tumor from the therapy experiment could be attributed to the fact that the therapy laser (1 kHz maximum repetition rate) missed some CTCs that were detected within 1 ms after the last therapy laser shot, which should not present a real problem since CTCs are rarer *in vivo* and the repetition rate of the therapy laser can be increased. The results indicated that our technique is capable of destroying CTCs with a high success rate, and that this therapy scheme is a promising way to impede metastasis for cancer therapy.

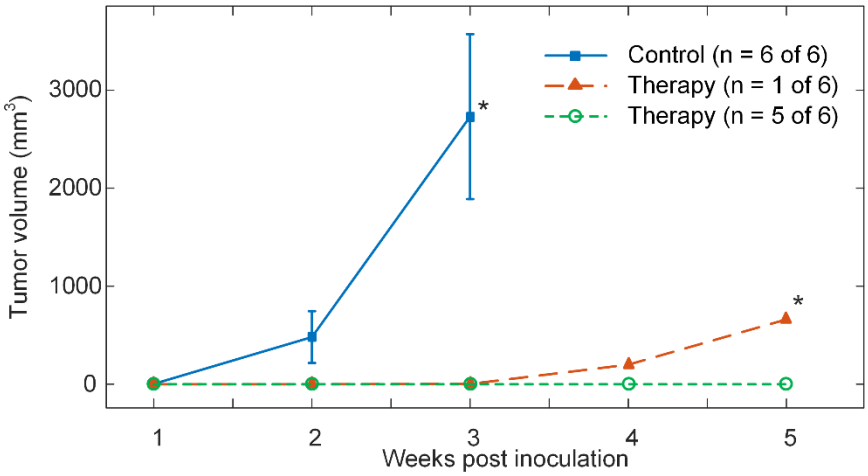

Figure 2.12 Comparison of tumor growth in the pseudo-therapy study. No tumor was detected using AR-PAM from five out of six therapy experiments by week 5 (green dashed line), and the only other therapy experiment resulted with a tumor that had a significantly slower growth (red dashed line), compared with that of the control experiments (blue solid line). Tumor volume was measured by AR-PAM (for flat tumors) or estimated by the formula $\pi/6 \times L \times W \times H$ (for raised tumors), where L, W, and H represent length, width, and height, respectively. Asterisk: mouse euthanasia; error bar: standard deviation.

2.4 Discussion

We report both *in vivo* label-free imaging of melanoma CTCs using dual-wavelength PA flow cytography and on-the-spot pinpoint CTC destruction by nanosecond-pulsed NIR therapy laser irradiation. CTCs are important indicators of the severity of a tumor and the efficacy of tumor therapies, making their reliable detection clinically significant. Because some CTCs are cloaked

by platelets or coagulation factors, they are shielded from many CTC detection agents as well as from the immune system[12, 18]. However, our method does not suffer from this limitation because light can penetrate CTCs. This technique may be used clinically for non-invasive *in vivo* CTC assays without labeling. In addition, many details about the process of tumor metastasis through CTCs are still unclear, and this high-resolution real-time CTC imaging technique can enable *in vivo* studies of CTC dynamics, such as monitoring tumor cells shedding from a primary tumor, invading nearby blood vessels, circulating in the vasculature, and extravasating from vascular walls.

Unlike therapeutics that use metastasis-specific features re-distribute the administered medication, the reported method works on a more selective "identify-then-locally-administer" basis. Because the radiant energy from the therapy laser is highly confined to the melanosomes within CTCs, other molecules in the CTCs, as well as adjacent RBCs, do not sustain damage. Moreover, our technology may have extra benefits in immunotherapy because it can help release viable tumor-specific antigens from lysed CTCs into vasculature, which can stimulate immune attacks on remaining CTCs as well as metastases, enhancing treatment efficacy[38]. Drug resistance from CTCs is also not an issue in our study because the destruction mechanism is completely physical.

Melanoma patients at all stages would potentially benefit from this technology if it were translated into the clinic successfully. For stages I and II, measuring CTC count could yield a more accurate diagnosis of a melanoma's recurrence risks. For stage III, when there are CTCs in the bloodstream but no existing metastases, and stage IV, when there are CTCs in the bloodstream and existing metastases, the clearance of CTCs would potentially prevent metastasis. The immunoresponse induced by antigens released by lysed CTCs could potentially further treat any residual primary tumor as well as existing metastases.

In summary, using endogenous contrast, our system dynamically imaged rare single CTCs and CTC clusters with single-cell resolution *in vivo* and performed real-time pinpoint photothermolysis of CTCs. The pseudo-therapy experiment demonstrated that our method can effectively kill CTCs in vasculature. This technology works in a convenient reflection mode, and is translatable to clinics. It can serve as a bedside therapy device for cancer patients, which can improve their prognosis by early detection and destruction of CTCs. The technology can also be applied for studying fundamental mechanisms of tumor metastasis through CTC dissemination.

Chapter 3: High-sensitivity photoacoustic flow cytography of circulating melanoma cells enabled by a 1 MHz Raman laser

Following the work in Chapter 2, this chapter continues the work on *in vivo* detection of CTCs. CTC is one of the key indicators of metastasis, which is responsible for the majority of cancer-related mortalities. Detection and characterization of CTCs *in vivo* can provide valuable information for cancer patients' diagnoses. Exploiting the intrinsic optical absorption contrast of melanin, we present a Raman-laser–based dual-wavelength high-speed photoacoustic (PA) flow cytography for imaging melanoma CTCs *in vivo*. Via the stimulated Raman scattering effect, a $KGd(WO_4)_2$ crystal works as a Raman shifter to convert 532 nm pump laser to 658 nm, at up to a 1 MHz repetition rate. Since melanin absorbs more than 100 times more strongly than hemoglobin at this wavelength, PA flow cytography can easily detect rare melanoma CTCs in the blood background, quantify their contrast-to-noise ratio, and measure their flow speeds. In mouse melanoma xenograft models, we have sequentially imaged the flow of rare CTCs *in vivo*. This PA flow cytography holds great promise for both tumor metastasis studies and clinical disease monitoring.

3.1 Background

Metastasis, the spreading of cancer cells from a primary tumor to distant sites, accounts for up to 90% of cancer-associated mortalities[10-12]. Most metastases involve the hematogenous dissemination of circulating tumor cells (CTCs)[11, 39], involving steps including cancer cells acquiring an invasive phenotype via mutations, entering the local blood vessels by intravasation, surviving in the blood circulation, extravasating through the vessel wall, and colonizing a new tumor[11, 21]. In this complicated process, rare CTCs, acting as cancer seeds, are key indicators of a

tumor's metastatic propensity[13, 40]. Thus, efficient detection and characterization of CTCs can provide critical information for cancer diagnosis and staging, and for assessing the efficacy of therapy[41-44].

Many recent studies employing various contrast mechanisms have enabled reliable CTC detection[17, 45]. However, the accuracy of *ex vivo* CTC assays is open to question because they depend on a small sample volume of blood[18]. *In vivo* CTC detection can improve sensitivity and reliability by accessing a larger portion of the total blood volume[17]. Many *in vivo* CTC detection studies that employ exogenous agents, such as fluorophore-labeled antibodies, have achieved promising results[21], but biosafety concerns impede their clinical translation[17, 45]. Thus, label-free detection of CTCs *in vivo* has attracted great interest.

In this work, we focus on CTC detection in melanoma, the deadliest type of skin cancer with a high propensity for metastasis at even an early stage[15, 29, 46]. Due to their high melanin expression, melanoma cells have a striking endogenous optical absorption contrast against the blood background in the red to near-infrared spectrum[22]. Hence, photoacoustic (PA) imaging, offering the highest possible sensitivity to absorption contrast and complying with the ANSI (American National Standards Institute) safety standard of skin exposure to laser, is a promising tool for *in vivo* detection and characterization of melanoma CTCs[6, 19].

In our previous work[9] (Chapter 2), we employed a non-optimal wavelength of 1064 nm for melanoma CTC detection, which was dictated by the wavelength availability of commercial high-repetition–rate lasers[47]. Within this constraint, stimulated Raman scattering (SRS) provides a convenient and efficient approach to implement multi-wavelength imaging[48, 49]. Through inelastic scattering of photons, this nonlinear process converts the pump laser into multiple discrete output wavelengths—Stokes lines[50]. As described in this letter, we employed a potassium gadolinium

tungstate crystal ($KGd(WO_4)_2$, or KGW), with a Raman shift at 901.5 cm^{-1}, to partially convert the 532 nm pump laser light to KGW's fourth Stokes line at 658 nm. At 658 nm, the ratio of the molar absorption coefficients of melanin to hemoglobin is at least 10 times higher than that at 1064 nm[22], significantly improving detection sensitivity. In addition, we achieved a laser pulse repetition rate of up to 1 MHz, owing to KGW's excellent thermal properties, including its high thermal conductivity, high damage threshold, and low thermal lensing[49]. Employing such a fast laser source, we report the development of high-speed dual-wavelength PA flow cytography that has successfully imaged the flow of rare single CTCs shed from melanoma xenografts in trunk blood vessels.

3.2 Methods

In our dual-wavelength PA flow cytography system (Figure 3.1), a 532 nm picosecond-pulsed laser (Olive-1064-4 BW, Huaray Precision Laser) was used both to pump the Raman laser and to provide the 532 nm imaging laser. In the Raman laser's path, the pump laser was loosely focused into the 30-mm-long KGW crystal (KGW-702, EKSMA OPTICS), and the SRS effect generated a series of Stokes lines (Figure 3.2a), described by $N\Delta\tilde{\nu} = (1/\lambda_p - 1/\lambda_{s_N})$. Here, $\Delta\tilde{\nu}$ is the Raman shift of the material, while λ_p and λ_{s_N} are the wavelengths of the pump laser and the Nth order Stokes line. Since KGW's Raman gain coefficient is dependent on the polarization of the pump laser, a half-wave plate (WPH05M-532, Thorlabs) was placed in front of the KGW to align the pump laser's polarization with the crystal's a-axis. The output beam was collimated and filtered by a band-pass filter (FBH660-10, Thorlabs) to selectively pass the fourth Stokes line at 658 nm. Since this high-order Stokes line had relatively large energy fluctuations (Figure 3.2b), it was sampled by a fast photodiode (PDA36A, Thorlabs) for pulse-to-pulse energy calibration. In the 532 nm path, the laser was sent through a 25-m long delay line, then combined with the 658 nm

laser by a dichroic mirror (Dichroic Laser Beam Combiner #86-393, Edmund Optics). The combined laser beams were focused by an achromatic convex lens (AC127-025-A, Thorlabs), and reflected to the tissue by a lab-made MEMS (micro-electro-mechanical systems) scanner. The laser energy was converted to acoustic waves through the optical absorption of endogenous absorbers and the subsequent thermoelastic expansion. The emitted PA waves were also reflected by the MEMS scanner, and then acquired by a polyvinylidene difluoride (PVDF) ultrasonic transducer (custom made by CAPISTRANO LABS: 40 MHz central frequency) which has a central hole for passing the laser beams. The MEMS scanner angularly steered both the laser beams and the PA wave in a confocal configuration during oscillation. Both the MEMS scanner and the PVDF transducer were immersed in a tank of deionized water for acoustic coupling.

The PA signals were amplified by a pair of radio-frequency amplifiers (ZFL-500LN+, Mini-circuits) and digitized by a data acquisition unit (ATS9350, Alazar Tech) at a 250-MHz sampling rate. For raster scanning, fast line scans were performed by the MEMS scanner at a 1 kHz rate (round-trip scanning at the 500 Hz resonance frequency), while slow orthogonal scans were provided by the motor stage (PLS-85 Precision Linear Stage, PI miCos GmbH) supporting the mouse. The 25-m delay line resulted in the 532 nm laser-induced PA signal arriving ~80 ns later than that from the 658 nm laser, which was sufficient to temporally resolve the two PA signals. The whole system was automated through a reconfigurable input/output module (NI PCI-7830R, National Instruments), and operated through an interface programed in LabVIEW. The maximal amplitude projection of the volumetric PA data was displayed in real time.

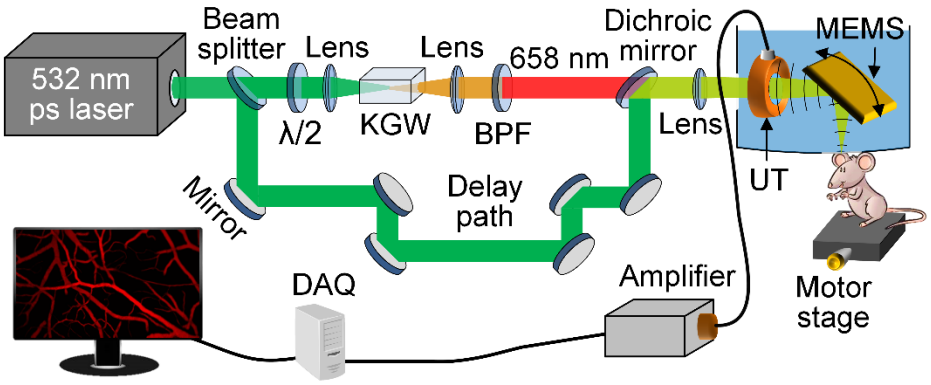

Figure 3.1 Schematic of the dual-wavelength high-speed PA flow cytography system. The 532 nm and 658 nm lasers are employed to image the vasculature and the melanoma CTCs, respectively. BPF, band-pass filter; DAQ, data acquisition unit; UT, PVDF ultrasonic transducer; λ/2, half-wave plate.

To quantify the performance of our Raman laser, first we used a spectrometer (AvaSpec-ULS2048XL-EVO, AVANTES) to measure its output spectrum (Figure 3.2a). The linewidth of the fourth Stokes line at 658 nm was 2.34 nm when producing ~100 nJ pulse energy at the 1 MHz repetition rate. After filtering the laser output with the band-pass filter, we measured the 658 nm energy output over 20 min (Figure 3.2b). The result indicated a relative standard deviation of 7.62% RMS (root mean square), which could be corrected by sampling every pulse with the photodiode. The beam profile captured with a CMOS (Complementary metal-oxide-semiconductor) camera (Grasshopper3 GS3-U3-23S6M, Point Grey) is shown in Figure 3.2c.

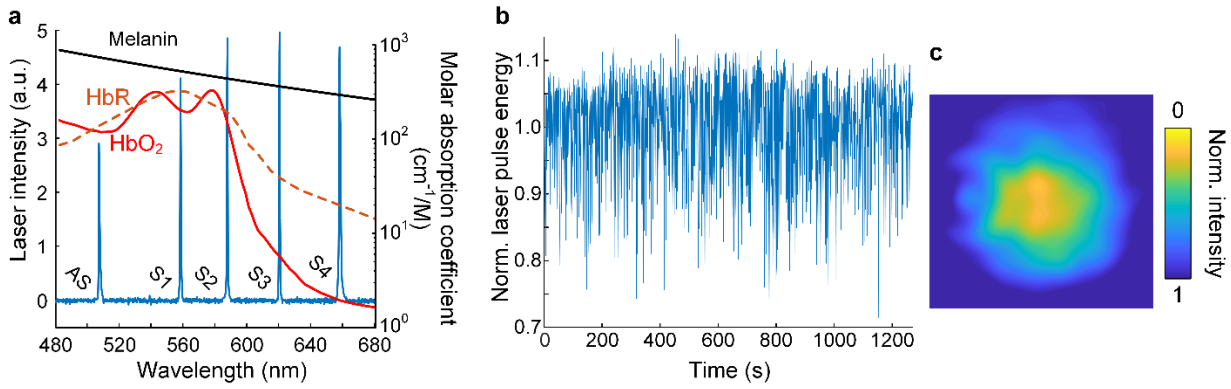

Figure 3.2 Performance of the Raman laser. (**a**) Optical spectrum of the multi-wavelength Raman laser output after filtering out the pump laser, plotted on a background of the oxy-hemoglobin (HbO_2), deoxy- hemoglobin (HbR), and

melanin absorption spectra. AS, the anti-Stokes line; S1–S4, the first to fourth Stokes lines. (**b**) Long-term stability measurement of the 658 nm Raman laser pulse energy. (**c**) Beam profile of the 658 nm Raman laser.

3.3 Results

To demonstrate our Raman laser-based PA flow cytography's capability to image melanoma CTCs on the fly, we imaged areas near a xenograft tumor in the mouse ear. Experiments were carried out in compliance with the laboratory animal protocols approved by the Institutional Animal Care and Use Committee of California Institute of Technology. A dose of ~10^4 B16F10 mouse melanoma cells was inoculated into the ear of an athymic nude mouse (Hsd:Athymic Nude-Foxn1^{nu}, Envigo) through intradermal injection (Figure 3.3ab). The B16F10 cell line was obtained from American Type Culture Collection, and was cultured in Dulbecco's Modified Eagle Medium, supplemented with 10% fetal bovine serum, at 37 °C in a humidified atmosphere with 5% CO_2. PA flow cytography first imaged the vasculature of the area near the tumor two weeks after inoculation (Figure 3.3c), and a region of interest (ROI) was further monitored for over 2 hours at a 20 Hz frame rate with a 2.7 μm lateral resolution. Owing to the strong absorption by the hemoglobin in red blood cells, the vascular structure was clearly imaged by the 532 nm laser. Exploiting the striking absorption contrast between melanin and hemoglobin, the 658 nm laser excitation of a single CTC produced a PA signal ~20 times stronger than blood, appearing as a hot spot in the dark background (Figure 3.3d). Figure 3.3e shows more snapshots of this CTC flowing in the artery. We performed control studies on normal mice and recorded no PA signals of a similar amplitude level, which verified that these PA signals indeed originated only from CTC absorption. The entire time course of this CTC flowing through the ROI was captured in a video. The arterial flow speed of this CTC was calculated to be 0.5 mm/s, which is in general accordance with previous reports.

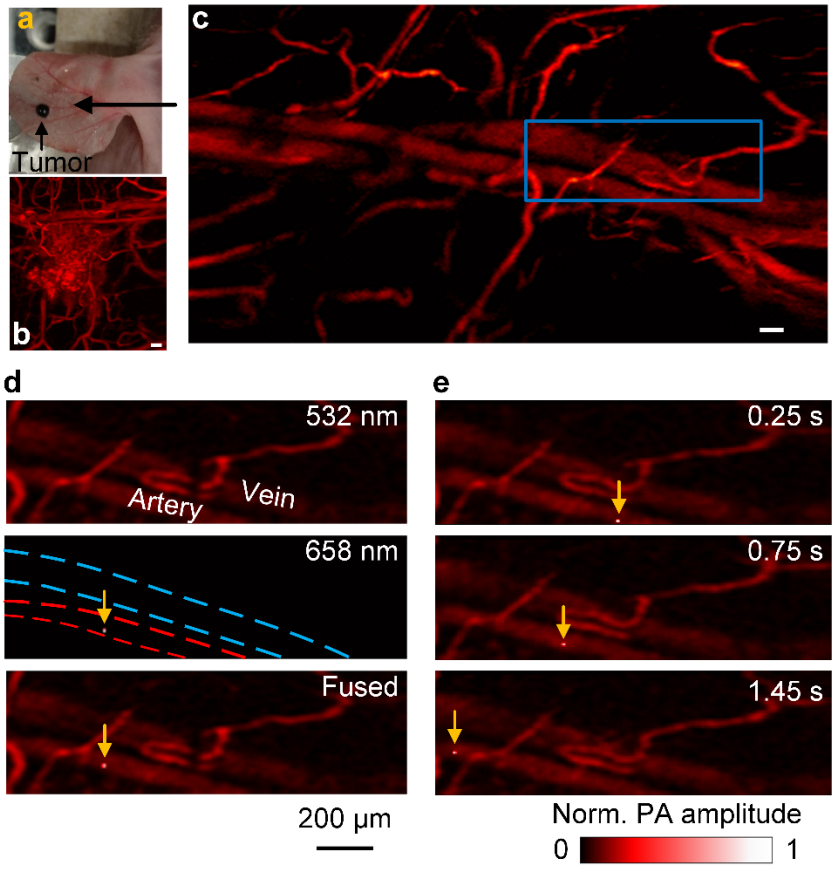

Figure 3.3 PA flow cytography of a melanoma CTC. (**a**) A photo of the melanoma model on the mouse ear at two weeks post inoculation. (**b**) PA image of the inoculated melanoma and its vascular environment at four days post inoculation. Scale bars in (**a**) and (**b**) represent 100 μm. (**c**) Flow cytography image of the vasculature near the tumor. The blue box indicates the ROI imaged at 20 Hz in the subsequent frames. (**d**) 532 nm laser-induced (top), 658 nm laser-induced (middle), and fused (bottom) flow cytography images showing a melanoma CTC flowing in the artery, as indicated by the yellow arrows. The CTC has a typical contrast-to-noise ratio of ~60. The trunk artery's and vein's boundaries are delineated by the red and blue dashed lines, respectively. (**e**) Three fused snapshots showing this CTC, illustrated by the yellow arrows, traveling in the artery. The labeled times are relative to the first frame containing this CTC.

3.4 Discussion

In summary, we report high-speed PA flow cytography based on a 1 MHz repetition rate Raman laser. Compared to our previous work in Chapter 2, we achieved a 4-fold improvement in the contrast-to-noise ratio, and a 5-times increase in imaging speed. This improvement enabled us to continuously monitor the flow of rare CTCs shed from tumor xenograft models *in vivo,* instead of coincidentally imaging CTCs only when they completely overlapped with the probing laser. This

PA flow cytography system complies with the ANSI safety standard, and is readily translatable to clinics. It can provide valuable information for predicting a melanoma's recurrence risk The Raman laser approach overcomes the wavelength limitation of the commercially available laser sources for high-speed multi-wavelength imaging. Compared to previously reported fiber-based Raman lasers, our free-space approach offers convenient system operation, adjustment, and upgrading. For example, by simply switching the 532 nm pump laser output to its fundamental mode at 1064 nm, this system can also perform multi-wavelength imaging in the near-infrared region, such as imaging lipid-rich neuron networks at 1177 nm and 1726 nm (the 1st and 4th Stokes lines of KGW when pumped at 1064 nm, respectively). It is also very easy to switch to other Raman materials with different wavelength outputs, such as barium nitrite ($Ba(NO_3)_2$, with a Raman shift at 1048.6 cm^{-1}), further extending the scope of this study. At present, we can achieve a sufficient imaging speed over only a relatively small field of view, so further work should address this limitation by employing techniques such as multi-focal imaging.

Chapter 4: Fast initial dip in mouse brains from a single stimulus imaged in single vessels by Raman-laser–based dual-wavelength high-speed functional photoacoustic microscopy

This chapter describes a new application of the wavelength conversion technique introduced in Chapter 3, stimulated Raman scattering, in the field of high-speed functional PAM. Considered as a spatiotemporally confined indicator for poststimulus neural activities, the initial dip holds great promise for neurological studies[51-53]. However, existing technologies still cannot fully reveal its detailed mechanism or profile, mainly because they failed to directly probe it at its microvascular origins[54]. Here we present Raman-laser–based dual-wavelength high-resolution functional photoacoustic microscopy (fPAM) that can image capillary-level hemodynamics at a 1 MHz one-dimensional imaging rate. We investigated the mouse brain vascular response to impulse forepaw stimulations, revealing a transient initial dip of blood oxygenation (sO_2) in cerebral micro-vessels starting as early as 0.13 s poststimulusly, preceding the total hemoglobin changes. The recovery from the initial dip and the subsequent sO_2 overshoot manifested a spatiotemporal pattern similar to the stimulation-activated hyperemic response, suggesting their close relations. Our fPAM sheds new light on this elusive initial dip phenomenon, and it is a valuable tool for functional studies requiring high spatiotemporal resolution.

4.1 Background

In the ongoing effort to decode our brain, functional imaging of small animals has been a hot topic in various biomedical imaging fields. Label-free imaging technologies often non-invasively probe

neural activities in an indirect manner[3, 55], such as measuring the stimulation-induced hyperemic response, which undergoes spatiotemporal broadening from neuronal activation sites[56, 57]. The initial dip, thought to be caused by increased oxygen consumption from activated neurons[51, 52, 58, 59], is considered to be a both spatially and temporally more confined localizer for the neural activity than the hyperemic response[57, 58, 60-62], and has attracted profound interest[63-67] since its discovery by diffuse optical spectroscopy[68]. Two label-free imaging techniques, functional magnetic resonance imaging[52, 65, 66] (fMRI) and wide-field optical microscopy[59, 60, 63], have both made valuable contributions to the understanding of the initial dip. However, small-animal fMRI lacks the spatial resolution to discern the dynamics of cerebral micro-vessels with diameters less than 50 μm[54], where the initial dip is thought to originate[57, 58]. Wide-field optical microscopy, in theory, has sufficient spatial resolution, but suffers from heavy round-trip optical scattering and low sensitivity when resolving deep vessels, because it relies on back-scattered photons from red blood cells[69] (RBCs). It also lacks the depth resolution[70]. As a result, the initial dip phenomenon is still not fully understood[52, 61, 64].

Label-free functional photoacoustic microscopy (fPAM), with optical diffraction-limited spatial resolution, offers unique advantages to overcome these bottlenecks[71], such as rich optical absorption contrast and volumetric imaging capability from single-plane scanning[3]. Through the photoacoustic (PA) effect[3], fPAM ultrasonically detects photons absorbed by endogenous absorbers, like hemoglobin in RBCs, thus making it more sensitive to hemodynamics than pure optical imaging because hemoglobin's optical absorption is much stronger than scattering. Also, since ultrasonic scattering in biological tissues is 2–3 orders of magnitude weaker than optical scattering[72], fPAM can achieve greater penetration depth than wide-field optical microscopy, enabling imaging the dynamics of deep cortical micro-vessels[3].

Here we report Raman-laser–based dual-wavelength fPAM employing the spectroscopic method for blood oxygen saturation (sO_2) measurement[73]. Conforming to the American National Standards Institute's (ANSI) safety standard, our fPAM has achieved high-sensitivity volumetric imaging at a 1 MHz one-dimensional (1D) rate with 2.7 μm lateral and 30 μm axial resolutions, revealing capillary-level cerebral vascular dynamics. We imaged the somatosensory area of mouse brains, and clearly observed a transient initial sO_2 dip from micro-vessels shortly after stimulating the forepaw. To the best of our knowledge, this is the first time that the initial dip has been directly imaged at the single-capillary scale, and our data provide new insights on this elusive phenomenon.

4.2 Methods

4.2.1 Raman laser

This section details the Raman laser technique first introduced in section 3.2. A Raman laser utilizes the SRS effect as the mechanism of light amplification. Stokes lines are generated by the pump laser through inelastic scattering. The energy difference between the pump photons and the scattered photons is fixed and related to a vibrational frequency of the Raman medium. Equation (4.1) is used to calculate the wavelength of the Nth order Stokes line[50]. Since the Raman shift, $\Delta\tilde{\nu}$, is generally reported in wavenumbers (cm^{-1}), unit conversion is explicitly expressed here:

$$N\Delta\tilde{\nu}(\mathrm{cm}^{-1}) = (1/\lambda_p\ (\mathrm{nm}) - 1/\lambda_{s_N}(\mathrm{nm})) \times (10^7\,\mathrm{nm/cm}) \qquad 4.1$$

where λ_p and λ_{s_N} are the wavelengths of the pump laser and the Nth order Stokes line, respectively. For a Raman crystal of a length of L and a Raman gain coefficient of g_R, the output power P_s of the first Stokes line is described as

$$P_s = \eta P_p \exp\left(\frac{P_p}{A_{\text{eff}}} g_R L_{\text{eff}} - \alpha_s L\right) \quad 4.2$$

where P_p is the power of the pump laser; A_{eff} is the effective area of the pump light incident on the crystal; $L_{\text{eff}} = (1 - \exp(\alpha_p L))/\alpha_p$ is the effective length of the crystal; and α_p and α_s are the crystal's attenuation coefficients for the pump laser and the first Stokes line, respectively. The term ηP_p represents the initial spontaneous Raman scattering at the input end of the crystal functioning as the seed for SRS, with η denoting the conversion rate. To achieve the SRS effect, the exponential term must be greater than 1, requiring a threshold of pump power at $P_{\text{th}} = \alpha_s L A_{\text{eff}}/g_R L_{\text{eff}}$. As seen in Equation (4.1), the energy conversion efficiency exponentially increases with pump intensity P_p/A_{eff}. However, for maximizing the output power and stability at the first Stokes line of 558 nm, its power should not exceed the threshold for generating the second Stokes line. Therefore, the pump intensity should be controlled within the following range[74]:

$$\frac{P_p}{A_{\text{eff}}} \in \left[\frac{\alpha_s L}{g_R L_{\text{eff}}}, \frac{30}{g_R L_{\text{eff}}}\right] \quad 4.3$$

where the upper limit is calculated by using a typical value of 10^{-7} for η.

4.2.2 MEMS scanner

This section describes the design and fabrication of a new MEMS scanner that has a better performance and smaller size than that in Chapter 2. This new torsional MEMS scanner consists of five major components: a 5 × 7 mm^2 mirror (custom made by Biomedical-Optics, silver coating and SiO_2 overcoating), a frame cut from a thin sheet of spring-tempered stainless steel (material and laser cutting provided by Potomac-laser), a permanent magnet (B222G-N52, K&J Magnetics), an inductor coil wrapped from 32 gauge magnet wires (Guasti Wire), and a hollow stainless steel mount for the assembly (custom made by eMachineShop) (Figure 4.1a). The frame consists of a

rectangular center plate of the same size as the mirror, two outer wings, and two hinges connecting the wings to the central plate. To assemble the scanner (Figure 4.1b), first, the mirror and the magnet were glued to the front and back sides of the frame's center plate, forming the scanning part. Second, the inductor coil was glued to the inner surface of the mount, forming the stationary part. Finally, the scanning part was fixed on the mount by fastening the frame's wings to the front surface of the mount. For underwater usage, marine grade epoxy was used to glue the components together. All components were centrally aligned during assembly, and the magnet's direction was aligned with the long side of the rectangular mirror.

The movement of the mirror is controlled by driving a sinusoid electrical current (provided through a differential amplifier: TDA7266 audio amplifier module, Shenzhen LC Technology) through the inductor coil (Figure 4.1c). In Newtonian mechanics, the resonance frequency f of the MEMS scanner can be calculated by solving a second-order differential equation obtained by Newton's second law and Hooke's law[75]:

$$K_s\theta = -I_m \mathrm{d}^2\theta/\mathrm{d}t^2 \qquad 4.4$$

where θ is the deflection angle of the hinge; K_s is the spring constant of the hinge, which is related to the hinge's structure and the torsional modulus of its material; and I_m is the moment of inertia of the scanning part, which is determined by its distribution of mass relative to the hinge. The solution of θ gives the scanner's resonance frequency f as

$$f = \frac{1}{2\pi}\sqrt{K_s/I_m} \qquad 4.5$$

Equation (4.5) assumes a friction-free operation. When the scanner works underwater, the resonance frequency f_{w} is described by

$$f_w = f\sqrt{1-\delta} \tag{4.6}$$

where δ is a damping factor related to the shape of the scanning part and the properties of water.

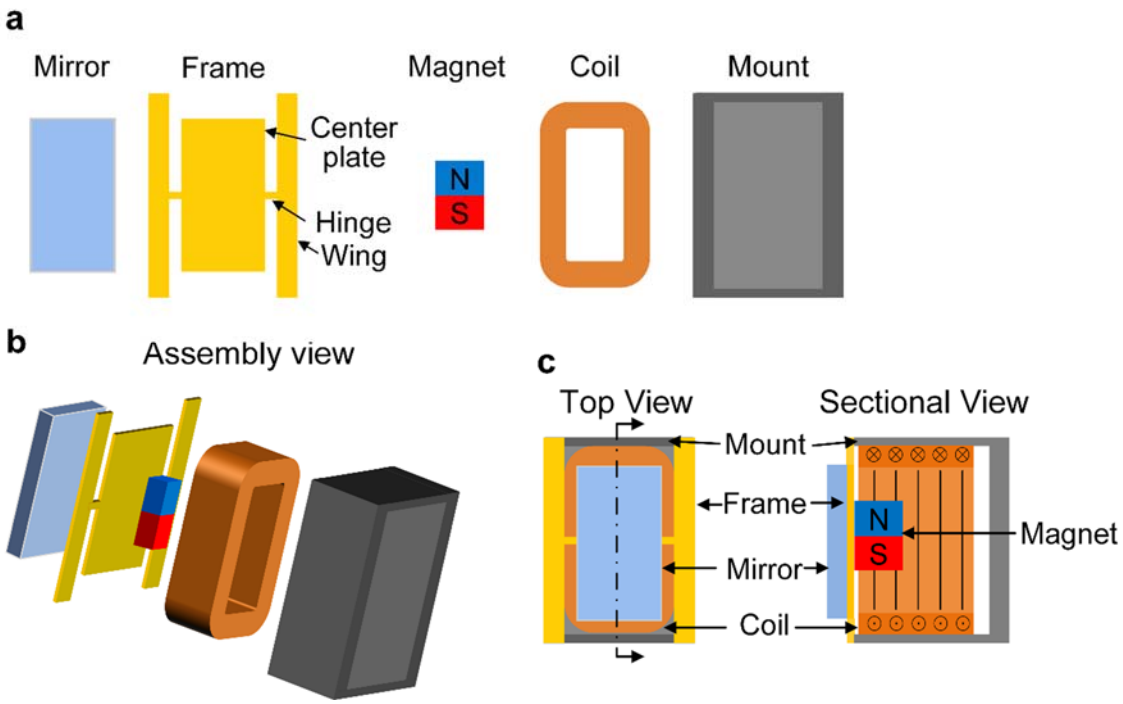

Figure 4.1 Schematic of the MEMS scanner. (**a**) Breakdown of the MEMS scanner. The scanning part of the scanner is comprised of the mirror, the center plate of the frame, and the permanent magnet. The stationary part is comprised of the two wings of the frame, the inductor coil, and the mount. The scanning part is connected to the stationary part via the two hinges of the frame. (**b**) Assembly view of the MEMS scanner. (**c**) Top and sectional views of the finished MEMS scanner. The actuation force is generated by the electromagnetic interaction between the electrical current through the inductor coil and the permanent magnet.

To achieve a desired resonance frequency, one may either adjust I_m by grinding the magnet to a certain thickness or adjust K_s by varying the structure of the hinge.

4.2.3 fPAM

The high-speed PAM system here employs a novel detection scheme with superior sensitivity compared to that in section 2.2. The details are described here. Two 532 nm picosecond-pulsed lasers (laser 1 in Figure 4.2a: Olive-1064-4 BW, Huaray Precision Laser; laser 2 in Figure 4.2a: APL-4000-1064, Attodyne Lasers) were employed in this dual-wavelength fPAM system, one

each for the 558 nm path and the 532 nm path, respectively. In the 558 nm path, the pump laser beam was loosely focused into the 30-mm-long KGW crystal (KGW-702, EKSMA OPTICS; b-cut), and the SRS effect partially converted the 532 nm pump photons to the first Stokes line at 558 nm. Since the Raman gain coefficient of KGW is dependent on the polarization of the pump laser, a zero-order half-wave plate (WPH05M-532, Thorlabs) was used to align the pump laser's polarization with the a-axis of the KGW crystal. The output beam was collimated by another lens and filtered by a band-pass filter (575/25 nm BrightLine, Semrock) to selectively pass the first Stokes line. In the 532 nm path, the laser beam was expanded and collimated by a pair of convex lenses. The 558 nm and 532 nm laser beams were combined by a dichroic mirror (Dichroic Laser Beam Combiner #86-393, Edmund Optics), focused by an achromatic lens (AC127-025-A-ML, Thorlabs), and reflected into the tissue by the lab-made MEMS scanner. PA waves excited by the laser pulses were also reflected by the MEMS scanner, and converted to electrical signals by a PVDF ultrasonic transducer (custom made by CAPISTRANO LABS: 40 MHz central frequency, 110% –6 dB bandwidth). Instead of using a complex optical-acoustic splitter, which has a low acoustic transmission efficiency, as in previous PAMs[9, 71, 76], we maintained the confocal configuration of the laser beams and the PA waves by passing the laser beams directly through the central hole of this ring-shaped PVDF transducer. Both the MEMS scanner and the transducer were immersed under deionized water in a water tank for acoustic coupling. The water tank, which had transparent windows on its side and bottom for light and acoustic wave transmission, was placed on top of the tissue with its bottom window in gentle contact with the acoustic gels applied on the tissue surface. The PA signals acquired by the transducer were then amplified by a pair of radio frequency amplifiers (ZFL-500LN+, Mini-circuits), and digitized by a fast data acquisition unit (ATS9350, Alazar Tech) at a 250-MHz sampling rate. For laser pulse energy calibration, a

photodiode (PDA36A, Thorlabs) was used to sample the laser beams, which were split by a wedged optical window (34-245, Edmunds Optics). The MEMS scanner was connected to a stepper motor, and the mouse was also supported by a motor-driven translation stage. For raster scanning, fast line scans were performed by the MEMS scanner at a 1 kHz rate (500 Hz resonance frequency), while slow orthogonal scans were provided by one of the two motors. The motor stage supporting the mouse was used for the wide-field-of-view (FOV) scanning (Figure 4.2e), and the stepper motor supporting the MEMS scanner was used for the narrow-FOV scanning. The system was automated by a field programmable gate array (NI PCI-7830R, National Instruments), and operated through an interface programmed in LabVIEW.

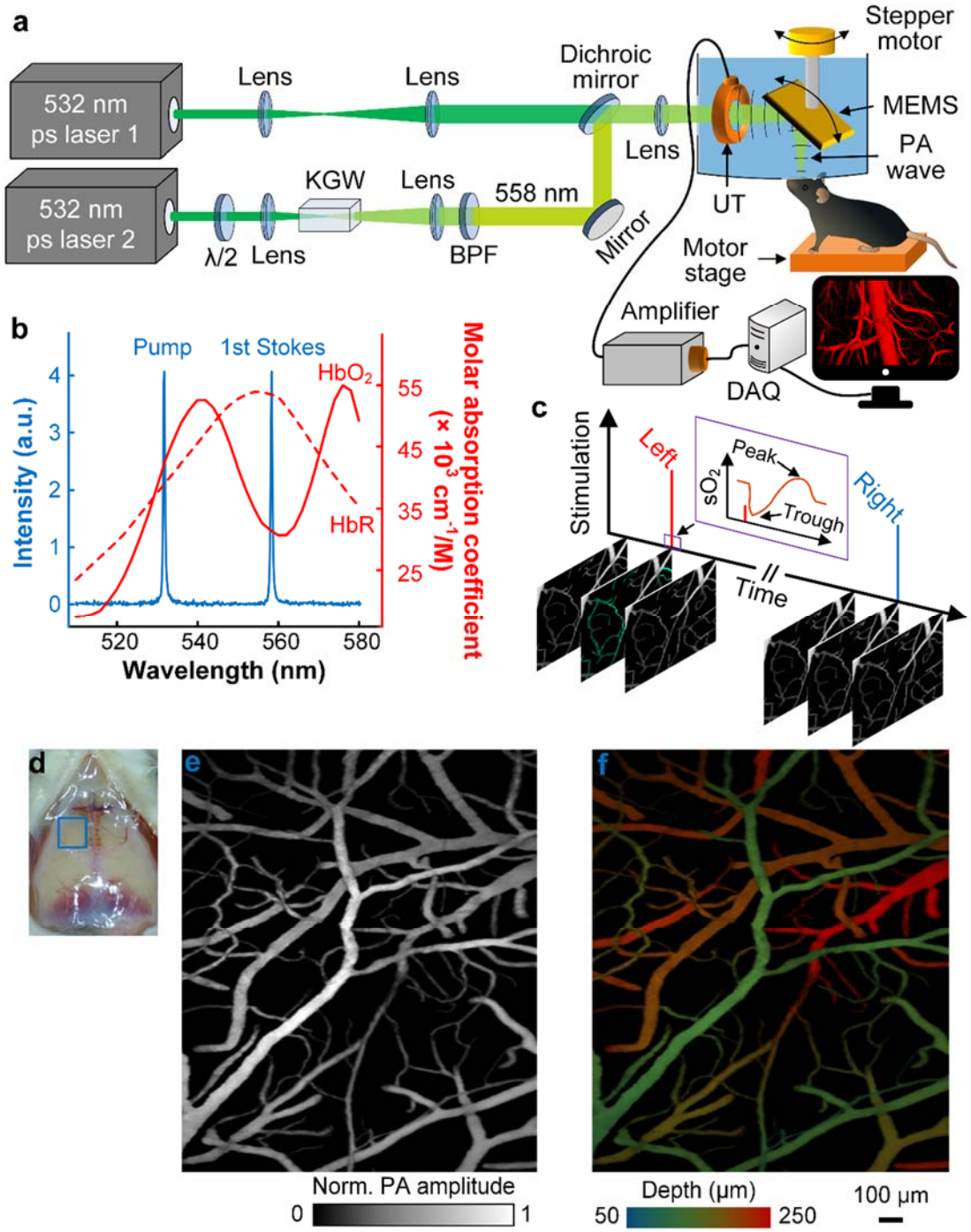

Figure 4.2 fPAM of the mouse brain. (**a**) Schematic of the fPAM system. λ/2: half-wave plate; BPF: band-pass filter; DAQ: data acquisition unit; UT: ultrasonic transducer. (**b**) Spectrum of the Raman laser plotted on the background of hemoglobin absorption spectra. HbO_2 and HbR: oxy- and deoxy-hemoglobin, respectively. (**c**) Scheme for the functional study. Imaging is performed continuously over an area in the somatosensory region enclosed by the blue square in **d**, while the mouse receives impulse stimulation to either one of its forepaws alternatingly. The stimulation-induced sO_2 response starts with a sharp decrease, the initial dip, followed by an overshoot (inset in **c**). (**e**) A representative MAP image of the somatosensory region. (**f**) The depth-encoded image of **e**.

In order to separate the two PA signals from the 532 nm and 558 nm laser pulses, Laser 2 was triggered 0.5 μs later than Laser 1. This 0.5-μs interval allowed the earlier PA wave to travel ~0.75 mm (greater than the maximum penetration depth of this fPAM system), and such a short interval also ensured that the two laser beams sufficiently overlapped in the focal plane during scanning.

The system's lateral resolution was optically defined at 2.7 μm. The axial resolution (along the acoustic axis) was ~30 μm, which was jointly determined by the laser pulse width, the frequency-dependent acoustic attenuation in tissue, and the frequency response of the ultrasonic transducer[77].

In our previous fPAM, the confocal alignment of the laser beams and the PA waves was achieved through an optical-acoustic splitter, which had a low efficiency for both optical and acoustic transmissions. Here, we circumvent this issue by employing a PVDF transducer with a hollow core for direct laser passage. The acoustic impedance of PVDF matches better with the tissue-coupling water than the piezoelectric ceramic transducer used in the previous version, which improves acoustic transmission efficiency. Further, PVDF transducers often offer a broader bandwidth than ceramic transducers, improving the axial resolution of PAM.

The sO_2 measurement in the previous work was based on optical absorption saturation, thus requiring a laser exposure exceeding the ANSI safety limit. Here, we employ the more established spectroscopic method for measuring sO_2. For *in vivo* brain imaging, the laser exposure on the tissue surface is 18 mJ/cm^2, within the ANSI standard, making it safe for future human imaging. Unlike several previously reported systems in which the scanners were made of proprietary materials or required expensive machining equipment, the MEMS scanner we developed here was fabricated

entirely from commercially available parts using common engineering tools, facilitating replication. We also achieved a 5-fold increase in imaging speed.

In summary, compared to the previous fPAM, our system's detection sensitivity is improved due to the low acoustic signal loss, despite the PVDF transducer being less sensitive than traditional ceramic transducers. The spectroscopic method employed here for the sO_2 measurement does not require optical absorption saturation. Therefore, our sO_2 mapping is also more robust, especially for deep vessels where the light attenuation is too strong to safely satisfy optical absorption saturation.

4.2.4 Data processing

We employed the Hessian-based vasculature enhancement filter to extract the blood vessels from our fPAM images[78]. The enhanced image was used to create a binary mask of vessels, which was applied to the raw images to remove non-vessel structures, such as residual blood stains on the brain.

The PA signal amplitude is linearly proportional to the local concentrations of oxy- and deoxy-hemoglobins, as described here[73]:

$$\begin{bmatrix} \mathrm{PA}_{532\ \mathrm{nm}}/\mathrm{F}_{532\ \mathrm{nm}} \\ \mathrm{PA}_{558\ \mathrm{nm}}/\mathrm{F}_{558\ \mathrm{nm}} \end{bmatrix} K = \begin{bmatrix} \varepsilon_{\mathrm{HbR}}(532\ \mathrm{nm}) & \varepsilon_{\mathrm{HbO_2}}(532\ \mathrm{nm}) \\ \varepsilon_{\mathrm{HbR}}(558\ \mathrm{nm}) & \varepsilon_{\mathrm{HbO_2}}(558\ \mathrm{nm}) \end{bmatrix} \begin{bmatrix} c_{\mathrm{HbR}} \\ c_{\mathrm{HbO_2}} \end{bmatrix}, \qquad 4.7$$

where PA represents the PA signal amplitude; F denotes the local optical fluence; ε is the molar absorption coefficient; c represents the local molar concentration; K is the system's proportionality coefficient relating the normalized PA signal to the absorption coefficient; and the subscript denotes the wavelength or the form of hemoglobin. Since K is unknown, only relative concentrations can be obtained. Least-squares fitting gives the solution as

$$\begin{bmatrix} c_{\mathrm{HbR}} \\ c_{\mathrm{HbO_2}} \end{bmatrix} = (M^T M)^{-1} M^T \begin{bmatrix} \mathrm{PA}_{532\ \mathrm{nm}}/\mathrm{F}_{532\ \mathrm{nm}} \\ \mathrm{PA}_{558\ \mathrm{nm}}/\mathrm{F}_{558\ \mathrm{nm}} \end{bmatrix} K, \mathrm{sO_2} = \frac{c_{\mathrm{HbO_2}}}{c_{\mathrm{HbO_2}} + c_{\mathrm{HbR}}}, \qquad 4.8$$

where M is the matrix in Equation (4.7).

The total hemoglobin concentration change was extracted from the 532 nm images, because this wavelength is an isosbestic point for the two forms of hemoglobin. Because dynamics caused by heartbeat were clearly evident from the PA traces, hemodynamic responses were extracted after low-pass filtering (Figure 4.3). Vessel diameters were measured as the shortest line across a vessel at different angles, with vessel boundaries identified using the 3σ threshold.

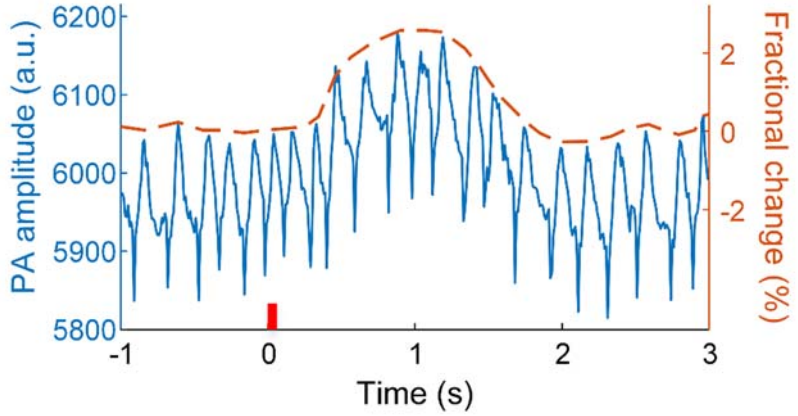

Figure 4.3 Extraction of total hemoglobin concentration changes. The blue line is the raw signal from line scans with the 532 nm laser. The fractional change, shown by the dashed line, is obtained by filtering out the heartbeat dynamics with low-pass filters. The red bar on the horizontal axis denotes the stimulus instant.

4.2.5 Experimental animals

Female ND4 Swiss Webster mice (Hsd:ND4, Envigo; 6–8 weeks old) were used for the animal experiment. The laboratory animal protocols were approved by the Institutional Animal Care and Use Committee of California Institute of Technology. First, the mouse was anesthetized with isoflurane, then taped to an animal holder with its head tightly fixed by a stereotaxic frame. Its body temperature was kept at 37 °C by a heating pad. Second, the scalp was surgically removed,

and the skull above the area roughly corresponding to the forepaw of the somatosensory cortex (S1FL region) was carefully thinned to a thickness of ~50 μm. Ultrasound gel was then applied on the brain to retain moisture and couple the acoustic waves. After the surgery, anesthesia was transferred to α-chloralose by an intraperitoneal injection of a dosage at 50 mg per kg body weight every two hours. Anesthesia depth was carefully controlled by monitoring the heart rate, respiration rate, and hindpaw pinch reflex. Next, a water tank filled with deionized water was placed on top of the mouse head. The plastic membrane at the bottom of the water tank was in gentle contact with the ultrasound gel applied on the brain. Finally, the mouse was placed under the fPAM for imaging. For high-frame-rate narrow-FOV imaging, as in Figure 4.8c, raster scanning was provided by the MEMS scanner and the stepper motor connected to the MEMS scanner. Therefore, the mouse remained in a natural motionless state.

4.2.6 Electrical stimulation protocol

Electrical stimulations were introduced by two pairs of needle electrodes inserted under the skin of the right and left forepaws. The electrodes were connected to a stimulator (Isolated Pulse Stimulator Model 2100, A-M Systems) for providing the electrical stimuli. A stimulation sequence consisted of a 60-s rest period, a single strong but brief electrical pulse to one of the forepaws, and a 50-s rest period. This electrical stimulus had an amplitude of ~2 mA and a pulse width of 40 ms. Next, the same stimulation was applied to the other forepaw (Figure 4.2c). This sequence was repeated five times, with a 1.0–1.5 min gap in between. The stimulation period and intensity were controlled without inducing noticeable motions. We employed a single brief stimulus instead of a pulse train since the initial dip is a fast response that can be confounded by multiple stimuli. Moreover, this stimulation scheme is also used in some other initial dip studies[59, 79].

4.3 Results

4.3.1 Imaging results

Our fPAM employs two laser wavelengths, 532 nm and 558 nm, to measure the vascular sO_2 in mouse brains (Figure 4.2a). We utilize a Raman crystal, potassium gadolinium tungstate ($KGd(WO_4)_2$, or KGW; Raman shift: 901.5 cm^{-1}), to convert a 532 nm picosecond-pulsed pump laser to KGW's first Stokes line at 558 nm through the SRS effect, with ~40% efficiency. The resulting 558 nm Raman laser has a linewidth of ~0.5 nm (Figure 4.2b) and a relative pulse energy deviation of 1.64% RMS (root mean square) when producing ~150 nJ pulses at a 1 MHz pulse repetition rate (Figure 4.4), indicating good monochromaticity and stability. A second 532 nm picosecond-pulsed laser provides the 532 nm laser beam. The two laser beams are combined and focused into the tissue to excite PA waves from hemoglobin in RBCs.

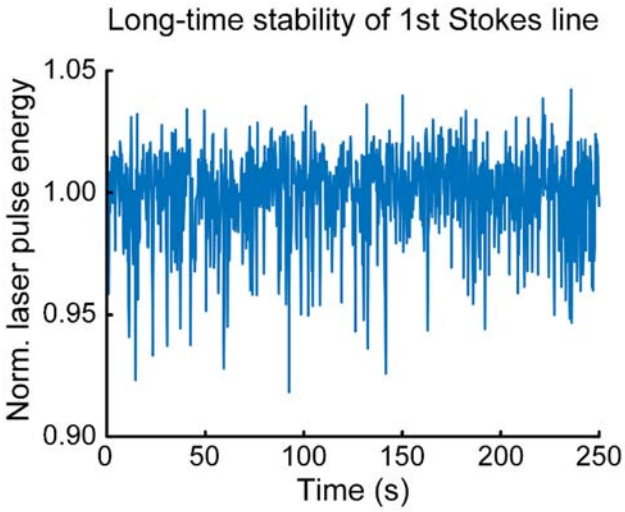

Figure 4.4 Stability test of the 558 nm first Stokes line output. The laser pulse energy was sampled by a high-speed photodiode (DET10A, Thorlabs).

To acquire the PA waves, we employ a ring-shaped piezoelectric polyvinylidene fluoride (PVDF) transducer that has a central hole for laser passage. During raster scanning, both the laser beams

and PA waves are confocally steered at up to a 1 kHz line scan rate by a lab-made MEMS (microelectromechanical system) scanner, assembled entirely from commercially available components (Figure 4.1). The PA signals acquired by the transducer are amplified by a pair of radio frequency amplifiers, then digitized by a data acquisition unit at up to a 1 MHz A-line rate. Maximum amplitude projection (MAP) images are displayed in real time.

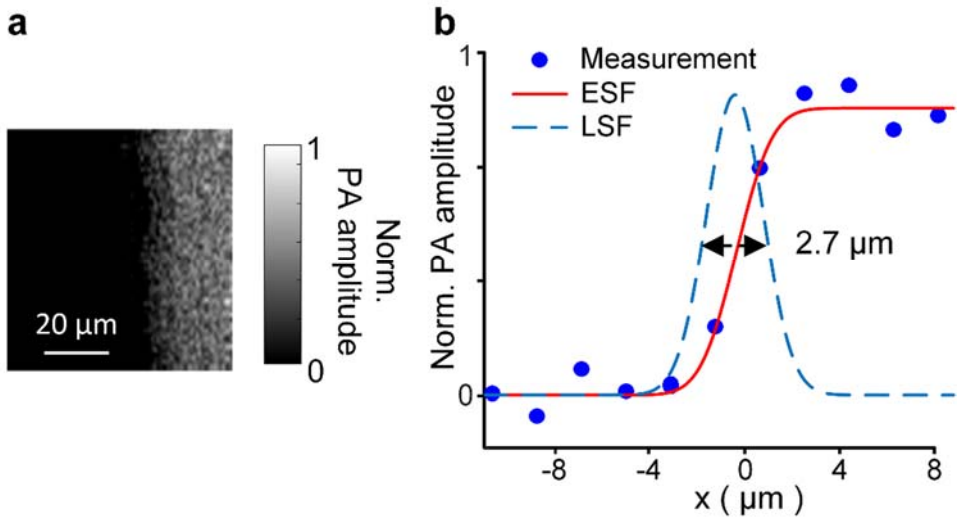

Figure 4.5 Lateral resolution measurement of fPAM. (**a**) PA image of a blade. (**b**) The edge spread function (ESF) is extracted by fitting the blade image data with an error function. The line spread function (LSF) is computed as the first derivative of the ESF. Lateral resolution is defined as the full width at half maximum of the LSF.

Our fPAM has achieved a lateral resolution of 2.7 µm (Figure 4.5) and a signal-to-noise ratio of 33.2 dB while imaging single RBCs in the cerebral vasculature through a thinned skull (Figure 4.6). The relative concentrations of oxy- and deoxy-hemoglobin are calculated by spectral analysis of the PA images acquired at 532 nm, a near isosbestic wavelength of hemoglobin, and at 558 nm, a nonisosbestic wavelength. Fractional changes in total hemoglobin concentration (HbT) are extracted from the images acquired at 532 nm (Figure 4.3).

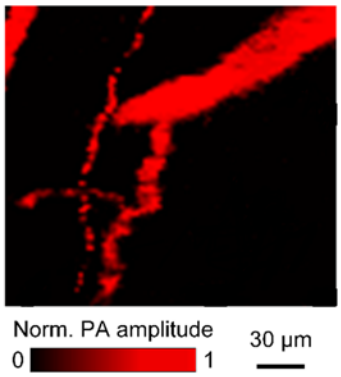

Figure 4.6 Imaging of cerebral blood vessels, showing individual RBCs. In this experiment, the mouse brain was pressed firmly against the membrane at the bottom of the water tank to facilitate discontinuous flows of RBCs.

Using our fPAM, we studied the mouse brain hemodynamic response to electrical stimulations by monitoring both sO_2 and HbT simultaneously (Figure 4.2c). First, we imaged over an area of the somatosensory cortex through a thinned skull (Figure 4.2de). We acquired 3D images with an imaging depth of up to 0.5 mm in a single raster scan (Figure 4.2f, and Figure 4.7).

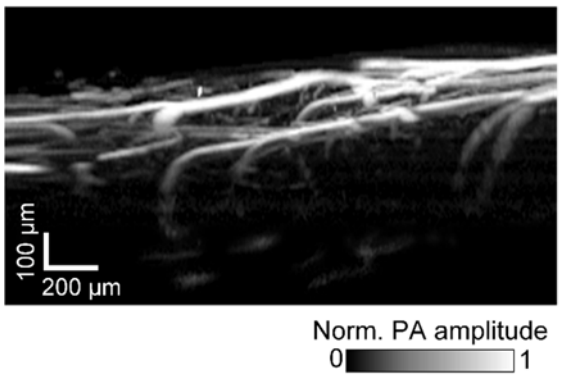

Figure 4.7 Representative PA image of cerebral vasculature projected onto the coronal plane. Volumetric data is obtained by single-plane scanning with the depth axis resolved by the times of flight of PA signals.

By fixing the optical focus at ~300 µm below the skull, the structure and oxygenation of capillaries as deep as Layer III of the cortex were clearly mapped (Figure 4.8a). In the resting state, the sO_2 in the micro-vessels decreased by ~15% per 100 µm along the vessel (Figure 4.8b), consistent with literature reports[6]. Next, a region of interest, illustrated by the blue square in Figure 4.8a, was monitored at a 6 Hz imaging rate while the mouse received brief electrical stimuli at its forepaws.

Our high-sensitivity and high-speed fPAM successfully resolved subtle and transient responses from micro-vessels.

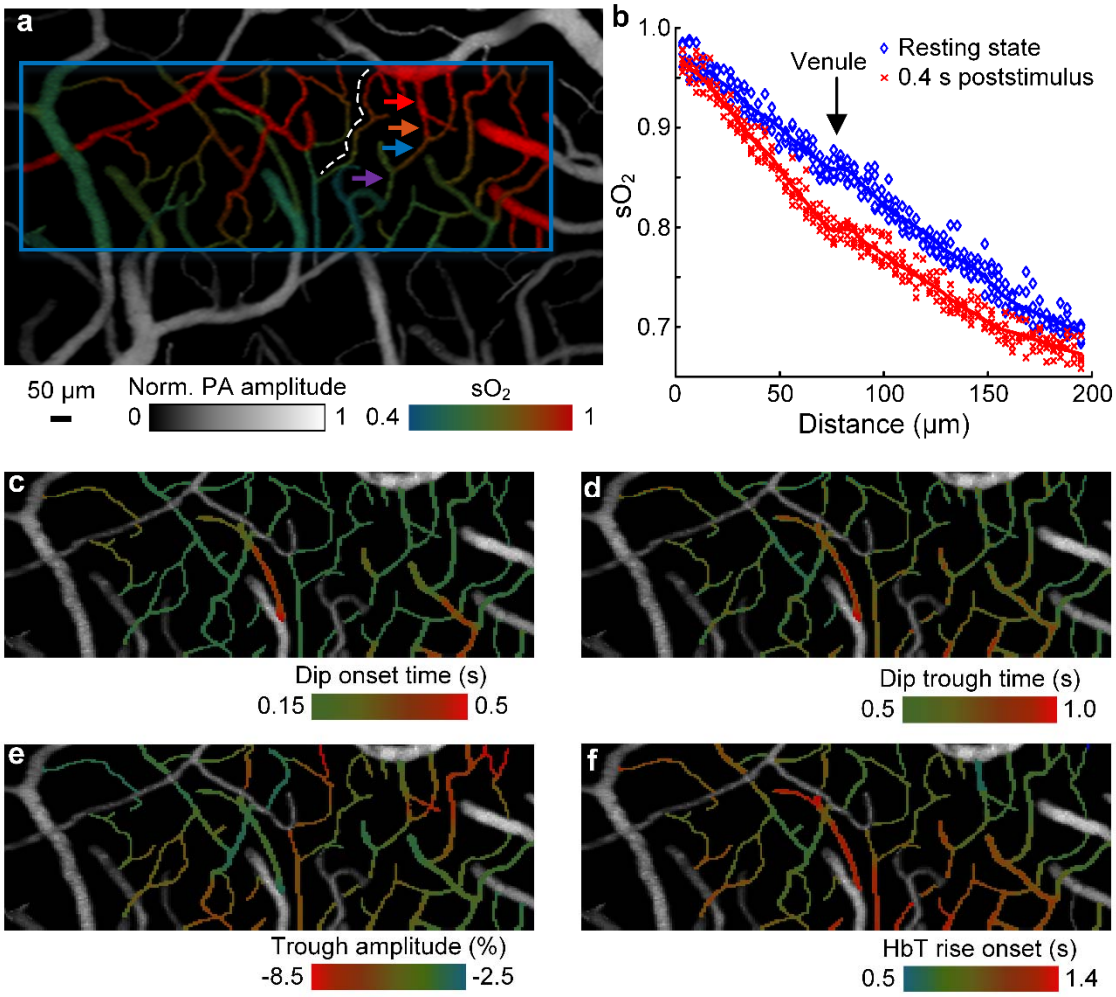

Figure 4.8 fPAM of cerebral vascular response to electrical stimulations. (**a**) sO_2 mapping of the somatosensory area in the resting state. The blue rectangle illustrates the region of interest for the subsequent functional imaging studies. (**b**) Oxygen release along a cerebral vessel marked with the white dashed line in **a**. A plateau, indicated by the arrow, is the site where the blood from another capillary flows into this vessel. (**c**) Timing of the initial dip onset (defined by 3σ) superimposed onto the grayscale structure image. (**d**) Timing of the initial dip trough. (**e**) Fractional change of the trough of the initial dip. (**f**) Timing of the hyperemic response onset. Data in (**c**–**f**) are averaged over five trials.

Upon contralateral stimulation, the sO_2 from capillaries, venules and small arterioles exhibited a two-phase response: a sharp and short decrease, then a recovery and a small overshoot. The hypoxic phase, the initial dip, started shortly after the stimulus nearly simultaneously across all

micro-vessels in the core response area (Figure 4.8c and Figure 4.9), but the trough of the initial dip demonstrated a propagation pattern from upstream arterioles to capillaries and further down to venules (Figure 4.8d). Similarly, the hyperoxic phase from upstream arterioles and capillaries notably preceded that of the downstream venules. Both the hypoxic and hyperoxic phases from capillaries had a greater fractional change than those from larger vessels (Figure 4.8e). The trough of the initial dip was followed by the hyperemia resulted from neurovascular coupling (Figure 4.8f), and its spatiotemporal distribution closely mirrored that of the hyperoxic phase. We also observed some arteriole dilation co-localized with the hyperemia.

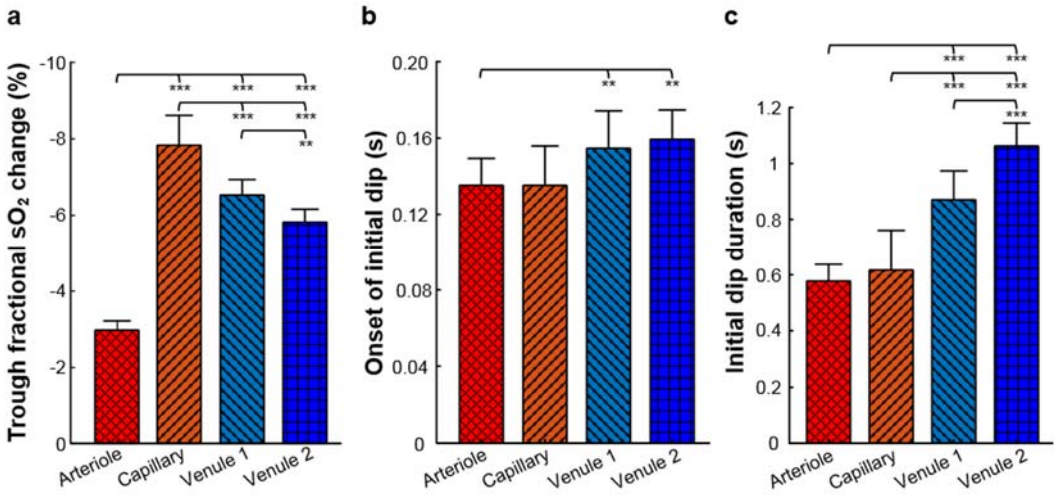

Figure 4.9 Statistical analysis of the hemodynamics in four vessel segments representative of the different microvascular compartments. Venule 1 and venule 2 denote postcapillary and second-stage venules, respectively. Data are averaged over five trials on each of the five mice; error bar, standard error; statistics, paired Student's *t*-test; *P* values, *** < 0.001; ** < 0.05.

4.3.2 Line scan results

Next, we performed fast line scans for 2D imaging across representative vessel segments from different microvascular compartments (arrows in Figure 4.8a) to acquire finer temporal profiles of the impulse response (Figure 4.10). Figure 4.10a shows a representative single-trial sO_2 response to an impulse somatic stimulation. The initial dip started first in capillaries (Figure 4.10b), with the onset time averaged over five mice being 0.13 ± 0.01 s (all time points are relative to the

beginning of the stimulus). The initial dip onset in other microvascular compartments occurred only up to 0.05 s later than that in capillaries, and it reached the trough at 0.4–0.7 s, with the trough from venules arriving ~0.3 s later than that from precapillary arterioles (Figure 4.10c). The capillary has a trough fractional change of up to 8%, which is more than twice that of the arteriole but only ~20% greater than that of the postcapillary venules (Figure 4.10d). Second-stage venules, the venules joined by postcapillary venules, also had an initial dip with a significantly longer duration than capillaries and arterioles, probably due to the out-of-phase influx of deoxygenated blood from different capillaries. Following the trough, the sO_2 levels quickly recovered, and capillaries and venules manifested a weak and flat overshoot, which was insignificant in arterioles (Figure 4.10c).

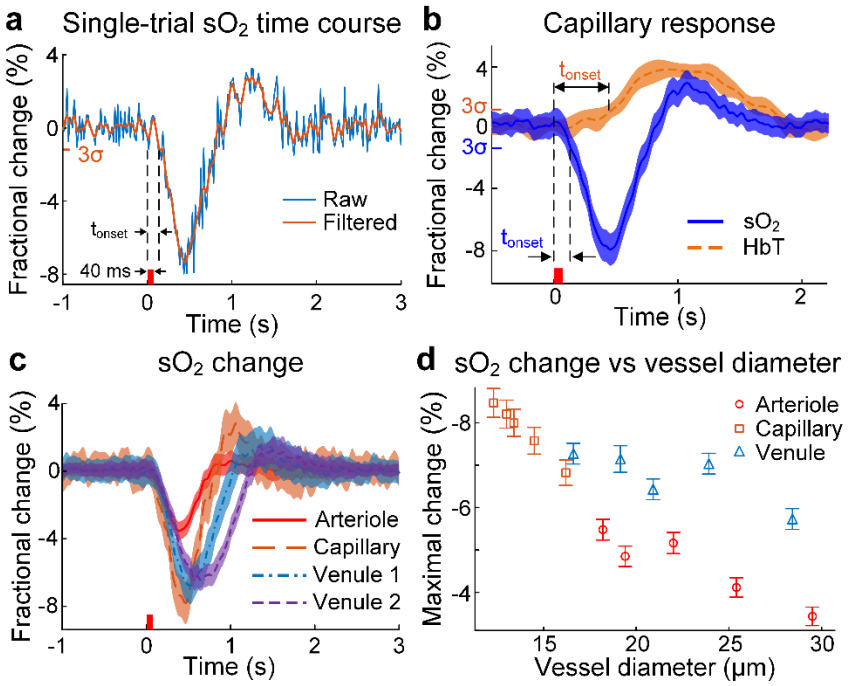

Figure 4.10 Temporal profiles of vascular response. (**a**) A representative single-trial capillary sO_2 time course in response to an impulse stimulus. The raw data (blue line) is filtered with a Bessel low-pass filter (25 Hz cutoff frequency) to produce the orange curve. We chose the Bessel filter because it preserves the wave shape of the filtered signal in the passband and therefore maintains causality. (**b**) Comparison of the time courses of sO_2 and HbT of the capillaries. By applying the threshold of 3σ, the onset times of the sO_2 and HbT responses are calculated as 0.13 and 0.46 s, respectively. (**c**) Time courses of the sO_2 fractional changes in four vessel segments representative of the

different microvascular compartments. An example of these representative segments is illustrated by the color-coded arrows in Figure 4.8a. (**d**) Initial dip amplitude versus vessel diameter for precapillary arterioles, capillaries, and postcapillary venules. Data in (**b** and **c**) are averaged over five trials on each of the five mice; data in (**d**) are averaged over five trials; the stimulus is illustrated by the small red bar on the horizontal axis; venule 1 and venule 2 denote postcapillary and second-stage venules, respectively; error bar shows standard error.

This overshoot phase lasted up to 2 s in venules. The hyperemia started first at the arteriole around 0.4 s, slightly ahead of the trough of the initial sO_2 dip in all compartments of the vessel (Figure 4.10b and Figure 4.11). Its peak amplitudes at the arteriole and capillary were similar, while venules had a weaker response but of a longer duration. The tail of hyperemia closely coincided with that of the overshoot phase of sO_2 response (Figure 4.10b), indicating a strong relation between them.

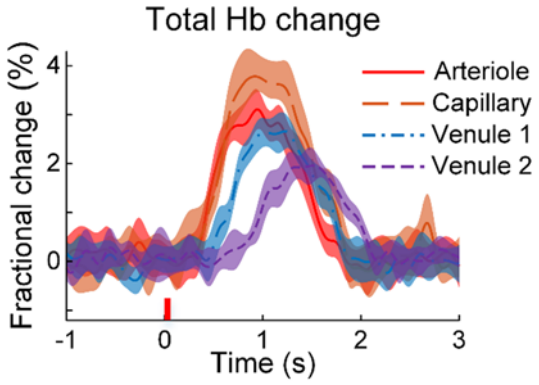

Figure 4.11 Time courses of the HbT fractional changes in four vessel segments representative of the different microvascular compartments. An example of these four stages is illustrated by the arrows in Figure 4.8a. Data are averaged over five trials on each of the five mice; the stimulus is illustrated by the small red bar on the horizontal axis; error bars show standard errors.

Meanwhile, the ipsilateral stimulation resulted in only a hyperoxic response in sO_2 and a hyperemia of a smaller amplitude, which occurred at a time point similar to that resulting from contralateral stimulations (Figure 4.12).

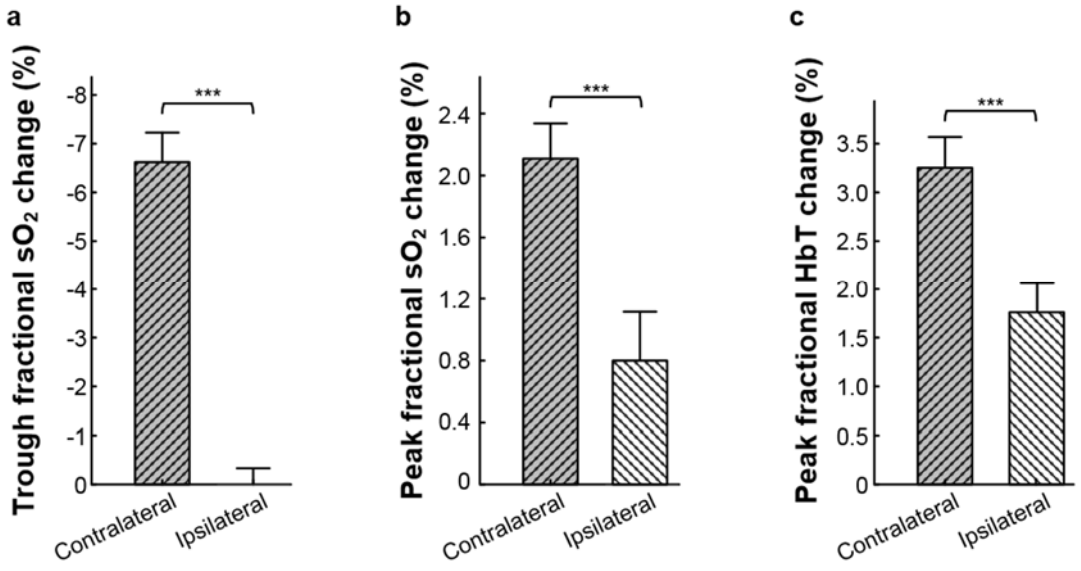

Figure 4.12 Comparison of vascular responses in the core response areas. (**a**) Trough amplitude of initial dips from contralateral and ipsilateral stimulations. (**b**) Peak value of the sO_2 overshoot. (**c**) Peak value of the hyperemic response. Data are averaged over five trials on each of the five mice; error bar, standard error; statistics, paired Student's *t*-test; *P* values, *** < 0.001.

4.4 Discussion

Since functional imaging often indirectly probes neural activities through measurements of hemodynamics, correct interpretation of the imaging data is crucial. Considerable research has been devoted to the initial dip, which is thought to be directly related to the local neural metabolism. However, despite being frequently observed and extensively studied by various imaging/spectroscopy modalities, its details remain inconclusive. Our experimental results provide a new and unique perspective on this initial dip phenomenon at high spatial and temporal resolutions. fPAM data showed that the initial sO_2 dip started as early as 0.13 s after the stimulus. Considering a typical value of ~4×10^{-5} cm^2/s for the oxygen diffusion constant in tissue[80], an extra-vascular hypoxic gradient would travel ~33 μm in 0.13 s, which is consistent with the general capillary density[81]. Excluding large venules that collect hypoxic blood, only vessels smaller than ~30 μm in diameter demonstrated a first-time initial dip, likely due to the ability to release oxygen. These two findings support the theory that the initial dip is the result of increased oxygen

consumption from activated neurons. Poststimulus hyperemia started slightly ahead of the trough of the initial dip, and propagated like the hyperoxic phase of the sO_2 response, likely contributing to the sO_2 recovery and overshoot.

Our motivation for developing a Raman laser was the limited choices of wavelengths for high-repetition-rate lasers[47, 82]. SRS effectively shifts the laser wavelength, with a conversion efficiency usually one order of magnitude higher than commercial optical parametric oscillator systems[83]. Compared to other popular Raman materials, KGW possesses many desirable features[49], such as convenient operation, a high Raman gain coefficient, a high thermal damage threshold, high thermal conductivity, and low thermal lensing, of which the last two factors are most critical for developing stable high-repetition-rate Raman lasers. Our free-space Raman laser also achieves better monochromaticity than fiber-based versions[84, 85]. The ultralow threshold of KGW enables the system to conduct simultaneous imaging at more than two wavelengths by employing additional higher-order Stokes and anti-Stokes lines. For example, melanoma progression and its hypoxia environment can be monitored by our fPAM working simultaneously at 532 nm, 558 nm, and 658 nm (4th Stokes line), further extending the scope of this study.

In summary, we developed a dual-wavelength fPAM based on a Raman laser at a 1 MHz 1D imaging rate. Through direct imaging of oxygenation in individual vessels with optical absorption-based contrast and high spatiotemporal resolution, fPAM achieved sensitivity and specificity superior to other imaging/spectroscopy modalities. We acquired detailed mapping of the hemodynamics at the micro-vessel level, which is unattainable for traditional optical imaging or fMRI. *In vivo* experiments quantified the transient initial dip from cerebral micro-vessels, providing new insights on this elusive phenomenon. Its multi-wavelength imaging capability may benefit many preclinical and clinical applications, such as tumor microenvironment studies.

Although advances in fPAM have opened avenues for *in vivo* biomedical studies, at present, our fPAM has a lower imaging speed than fMRI or optical microscopy for wide-field imaging, and future studies should address this issue by exploiting techniques like multi-focal imaging. Imaging awake animals with a wearable version of fPAM can be another important avenue of exploration.

Chapter 5: Transparent high-frequency ultrasonic transducer for photoacoustic microscopy application

Chapter 4 introduces a high-speed dual-wavelength fPAM system for functional imaging of the mouse brain. This system successfully resolved transient hemodynamic changes on a single micro-vessel level. However, limited by its sizable optical scanning and ultrasonic detection devices, its applications are limited to imaging anesthetized animals. Moreover, anesthetics are found to have some profound effect on brain activities[86, 87]. Thus, there is a need for microscopy technologies capable of imaging hemodynamics in awake animals in order to study the natural brain activities. Among potential solutions, wearable microscopes present a promising approach. In this work, we report development of a thin-film optically transparent high-frequency ultrasonic transducer using lithium niobate single-crystal and indium-tin-oxide electrodes, presenting an excellent optical transparency of up to 90% in the visible to near infrared spectrum. The center frequency of the transducer was at 36.9 MHz with 33.9% –6 dB fractional bandwidth. Imaging capability of the fabricated transducer for photoacoustic microscopy was also demonstrated by successfully imaging a resolution target and mouse ear vasculature *in vivo*, which were irradiated by a 532 nm pulsed laser transmitted through the transducer. This transparent transducer holds great promise for wearable PAM applications. This work was done in collaboration with Dr Qifa Zhou's lab in University of Southern California.

5.1 Background

Photoacoustic tomography (PAT) remains the prime choice for label-free imaging of the optical absorption contrast in tissue[3, 4, 88]. It can extract the three-dimensional information of a wide range of endogenous absorbers, such as hemoglobin, melanin and cytochrome[4]. To construct the

absorption-based images, PAT detects the ultrasonic waves converted from absorbed optical energy through thermoelastic expansion[2, 3]. Photoacoustic microscopy (PAM), the microscopic version of PAT, usually employs a single high-frequency ultrasonic transducer to acquire the photoacoustic waves[2]. So far, the most widely used PAMs for *in vivo* animal and human imaging utilize a reflection-mode setup: both the optical illumination and ultrasonic detection placed on the same side of the imaging object[6, 7, 9, 71]. However, this setup imposes certain constraints on PAM's performance. A long working distance is required to accommodate the sizeable piezoelectric detector and the optical-acoustic splitter, thus limiting the PAM's numerical aperture and resulting in a poor lateral resolution[76, 89]. Transmission-mode PAMs have achieved finer lateral resolutions, but they are mainly limited to imaging *ex vivo* samples[90, 91]. Further, the complexed optical-acoustic splitter, two prisms sandwiching a thin layer of silicon oil, is very difficult to make and maintain[76, 89].

To address this problem, doughnut-shaped transducers with a central opening for light passage have been introduced to reduce the obstruction in the optical path[7, 92]. But its size is still too big for PAM to achieve a resolution comparable to optical microscopy[92]. Taking another approach, thin-film transducers that are optically transparent offer a desirable solution. One type of these transducer is the optic-based ultrasonic detectors, including Fabry-Perot etalons[93, 94], micro-ring resonators, and others[95]. However, they require additional optical instruments such as probe lasers and detectors. Further, it is difficult to integrate these optical-based detection techniques with conventional ultrasound excitation device for combined ultrasound/photoacoustic dual-modality imaging. Although transparent piezoelectric transducers with indium-tin-oxide (ITO) coated polyvinylidene fluoride (PVDF) film were already introduced[96, 97], they demonstrated only 70% ~ 80% transparency in the visible spectrum. Also, PVDF's coupling coefficient (k_t) is not

comparable with other popular piezoelectric materials. Another alternative was developed using the capacitive micromachined ultrasonic transducer (CMUT) technique[98]. This device has limitation on operating frequency and complex configuration that utilizes specialized micro-electro-mechanical systems (MEMS) fabrication techniques.

Moreover, transducers operating at the range of 30-50 MHz are favorable for PAM imaging, since the frequency spectrum of PA waves after propagating through tissue is dominant in this range[71]. Therefore, there is a need to find a suitable piezoelectric material to develop optically transparent high-frequency ultrasonic transducers for PAM application.

Among known piezoelectric materials, lithium niobate ($LiNbO_3$) possesses several properties ideal for fabricating transparent high-frequency ultrasonic transducers: It is a single-crystal material with excellent transparency at wavelength from 350 to 5200 nm[99], good electromechanical coupling, a low dielectric constant, and high longitudinal sound speed, ideal for designing sensitive large-aperture high-frequency transducers. A brief list of the material properties for $LiNbO_3$ can be found in [100]. Beard et al. developed an optically transparent piezoelectric transducer with ITO coated $LiNbO_3$ for ultrasonic particle manipulation[101]. Recently, Dangi et al. reported a promising $LiNbO_3$-based transparent ultrasonic transducer operating at 14.5 MHz for PA imaging[102].

The purpose of this study is to develop a transducer for PAM applications with a high optical transmission (> 80 %) and a high frequency (> 30 MHz) response. The high transmission of $LiNbO_3$ single-crystal substrate coated with ITO thin films on both sides is demonstrated over a broad range of wavelengths (450-1064 nm). PAM imaging performance of the transparent transducer is evaluated by imaging a carbon nanotube-based resolution target and mouse ear vasculatures *in vivo*.

5.2 Materials and methods

5.2.1 Transducer design

A Krimboltz, Leedom, and Mattaei (KLM) transducer equivalent circuit model-based modeling software (PiezoCAD, Sonic Concepts, Woodinville, WA, USA) was used to simulate and optimize the transducer design. Parylene thin-film (Parylene C, Specialty Coating Systems, Indianapolis, IN, USA) with an acoustic impedance of 2.5 MRayl was selected as the material for the matching layer because it exhibits very little absorption in the visible region and is, therefore, transparent and colorless. To facilitate transducer transparency, an insulating and optically transparent epoxy (EPO-TEK 301, Epoxy Technology, Inc., Billerica, MA, USA) with an acoustic impedance of 3.05 MRayl was chosen as the material for backing.

Table 5.1 Design parameters of the transparent high-frequency ultrasonic transducer

Specifications	Values
Designed center frequency	37 MHz
Aperture size	1 cm × 1 cm
Thickness of piezoelectric material ($LiNbO_3$)	100 μm
Thickness of matching layer (parylene)	16 μm
Thickness of backing (EPO-TEK 301)	1 mm

Design parameters of the transducer are summarized in Table 5.1. The inner structure cross section schematic of the transducer is shown in Figure 5.1a.

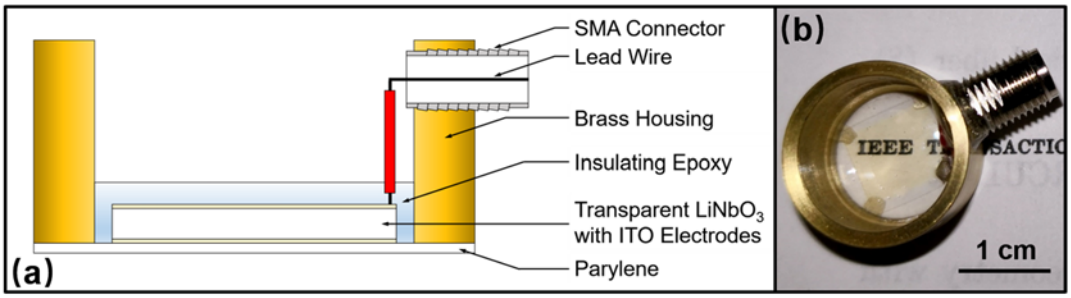

Figure 5.1 Schematic and photo of the transparent transducer. (**a**) Design cross section of the transparent ultrasonic transducer (not to scale). (**b**) photograph of a fabricated transparent ultrasonic transducer.

5.2.2 Transducer fabrication

A 36° rotated Y-cut $LiNbO_3$ (Boston Piezo-optics, Bellingham, MA) wafer with a dimension of 1 cm × 1 cm and a thickness of 100 μm (λ/2) was acquired to make transducer operating at 37 MHz. Transparency of the $LiNbO_3$ wafer was achieved by chemical surface finish technique. Both top and bottom sides of the $LiNbO_3$ wafer were electroded by sputtering an ITO layer of approximately 108 nm in total thickness. ITO was DC magnetron sputtered from a 50 mm diameter ITO target (In_2O_3/SnO_2 90/10 wt %, Kurt J. Lesker Company, Jefferson Hills, PA, USA) at 20 W, 933 Pa (7 mTorr, Argon flow ≈ 30 sccm) for 80 minutes. The deposition rate was monitored using a quartz crystal microbalance (QCM) with a measured rate of 0.03 nm/s (density = 7.14 g/cm^3, z-ratio = 1, tooling = 100 %). For an accurate measure of on-sample deposition rate ($LiNbO_3$ crystals and QCM are at differing heights), ITO was sputtered on a silicon substrate under similar conditions for 20 min and measured using a white light spectrometer (Filmetrics F40, KLA, Milpitas, CA, USA). The 20 min sputtered film yielded a refractive index of 1.89 and a thickness of 27 nm. Extrapolating these values, we estimate the thickness of the ITO film on the $LiNbO_3$ to be 108 nm. A hook-up wire (Gauge 24, McMaster-Carr Supply Company, Santa Fe Springs, CA, USA) consisting of stranded copper wires was connected to the bottom ITO electrode on the edge of the $LiNbO_3$ wafer with a small amount of conductive epoxy (E-SOLDER 3022, Von Roll Isola Inc., New Haven, CT, USA). A home-made brass housing with an inner opening of 15 mm in diameter

and a subminiature version A (SMA) connector on the side was placed concentrically with the $LiNbO_3$ wafer. The other end of the stranded copper wire was connected to the SMA connector. Degassed EPO-TEK 301 with a total weight of 0.2 g was then poured into the brass housing. Therefore, the thickness of EPO-TEK 301 was controlled to be approximately 1 mm after curing. A small amount of E-SOLDER 3022 was applied at the four corners on the front surface of the $LiNbO_3$ wafer to connect the top ITO electrode with brass housing as a ground connection. Finally, a 16 μm thick (λ/4) parylene thin-film (Parylene C, Specialty Coating Systems, Indianapolis, IN, USA) layer was vapor-deposited onto the external surface of the transducer by a parylene coater (PDS 2010, Specialty Coating Systems, Indianapolis, IN, USA). Photograph of the fabricated transducer is shown in Figure 5.1b. The transducer was not focused by either press-focusing or lens focusing techniques.

5.2.3 PAM imaging

To demonstrate applications in PAM, we conducted phantom and animal imaging with a reflection-mode PAM (Figure 5.2a). The laser beam from a pulsed laser (APL-4000-1064, Attodyne Inc., Toronto, ON, Canada) was focused onto the imaging object by an aspherical lens (AL2550-A, Thorlabs Inc., Newton, NJ, USA), through the transparent transducer. Excited PA waves were detected by the transparent transducer, which was placed in a tank of deionized water for acoustic coupling. Maximum amplitude projection (MAP) images were produced in post-processing by taking the peak-to-peak amplitude of each PA A-line signal.

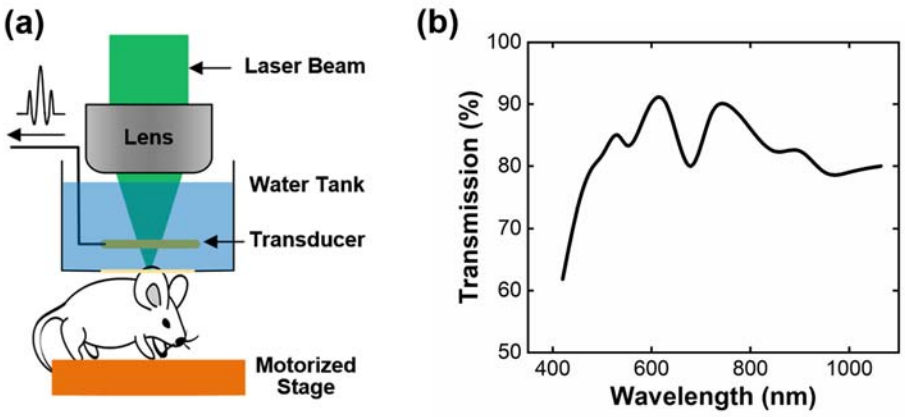

Figure 5.2 Schematic of the PAM setup and transparency measurement of the transducer. (a) Schematic of the reflection-mode PAM. The transparent transducer, directly in the optical path, is placed on the top of the imaging object to acquire the excited PA waves. The imaging object was mounted on a motorized stage for raster scans; (b) Measurement of optical transmission through the fabricated transducer.

5.3 Results

5.3.1 Transducer performance evaluations

First, we evaluated the transducer's optical transmission efficiency. An optical parametric oscillator laser (NT242, EKSPLA, Vilnius, Lithuania) provided the laser beams at a broad spectrum, and the ratio of the laser light transmitted through the transducer was measured with a laser power meter (Vega, Ophir Optronics Solutions Ltd., Jerusalem, Israel). It can be seen that our transducer has a transmission efficiency greater than 80% in the 450 nm to 1064 nm range (Figure 5.2b).

Electrical impedance of the transducer was measured by an impedance analyzer (HP 4294A, Agilent Technologies, Santa Clara, CA, USA). Electrical impedance and phase angle of the transducer as a function of frequency were measured and shown in Figure 5.3b. The resonance frequency (f_r) and anti-resonance frequency (f_a) of the transducer were measured to be 33.9 and 40.3 MHz, respectively. According to the IEEE standard on piezoelectricity[103], the effective electromechanical coupling coefficient (k_{eff}) of the transducer was calculated to be 0.54. It was

observed that the measured results are very close to the PiezoCAD simulation results (f_r = 31.0 MHz, f_a = 37.8 MHz, and k_{eff} = 0.57) as shown in Figure 5.3a. The electrical impedance of the transducer was measured in the range of 161 to 258 Ω around the resonance frequency of the transducer, while the PiezoCAD simulation shown 7 to 22 Ω.

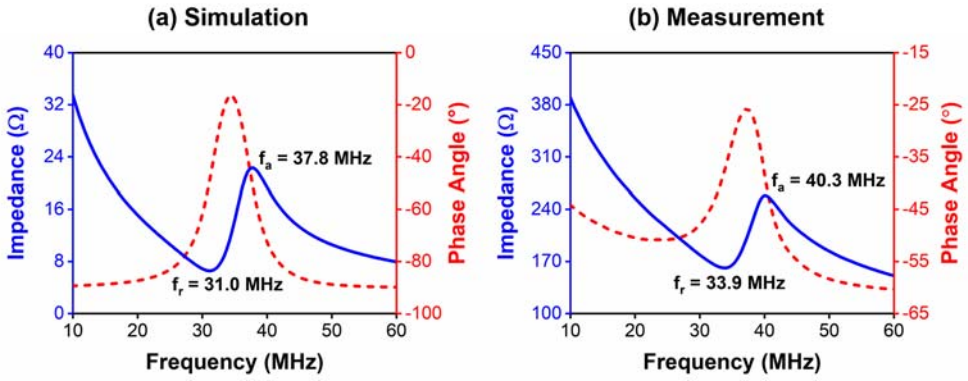

Figure 5.3 Data of the transducer impedance. (**a**) PiezoCAD simulated and (**b**) measured electrical impedance (blue) and phase angle (red) of a transparent transducer.

Pulse-echo response of the transducer was measured and analyzed by a pulse-echo method described in[104]: The transducer was mounted on a holder and immersed in a tank filled with deionized water. An X-cut quartz plate was placed about 5 mm away from the transducer as a reflector. The transducer was excited by a pulser-receiver (Panametrics 5900PR, Olympus NDT Inc., Waltham, MA, USA) with 1 μJ energy per pulse, 200 Hz pulse repetition rate, and 50 Ω damping factor. The received pulse-echo response and its computed frequency spectrum are shown in Figure 5.4b. The center frequency of the transducer was calculated to be 36.9 MHz, and the -6 dB bandwidth was 33.9%. Peak-to-peak received voltage ($V_{p\text{-}p}$) of the unamplified pulse-echo signal was about 0.45 V, indicating the transducer has quite high sensitivity. The measured pulse-echo results are in good agreement with the PiezoCAD simulation Figure 5.4a.

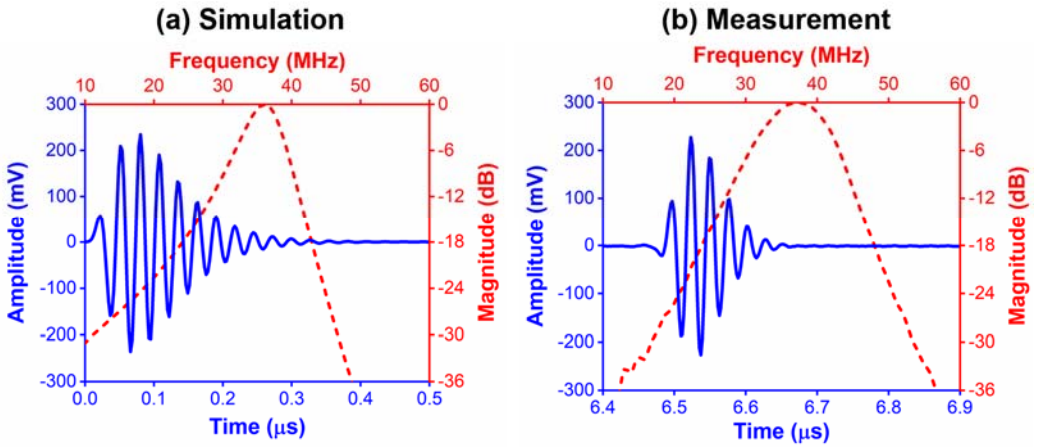

Figure 5.4 Data of the transducer's impulse response. (**a**) PiezoCAD simulated and (**b**) measured pulse-echo response waveform (blue) and its frequency spectrum (red) of a transparent transducer.

5.3.2 PAM imaging

Figure 5.5a shows the PAM image of the resolution target, carbon-nanotube patterns grown on a polydimethylsiloxane substrate. The smallest pattern, periodic lines of 10 μm width, 100 μm long, and 40 μm pitch were clearly resolved. The laser pulse energy irradiated on the target was measured to be ~200 nJ, resulting a signal-to-noise ratio of ~41.5. Further, we demonstrated the transparent transducer's *in vivo* imaging capability by imaging the mouse ear at the optical wavelength of 532 nm. At this wavelength, the hemoglobin in red blood cells (RBCs) is the primary absorber in tissue, thus enabling imaging the vascular anatomy. The laboratory animal protocols were approved by the Institutional Animal Care and Use Committee of California Institute of Technology. Figure 5.4b shows the MAP image of a 1 × 0.8 mm^2 area of the mouse ear. It can be seen that vessels of a diameter as small as 30 μm were clearly imaged.

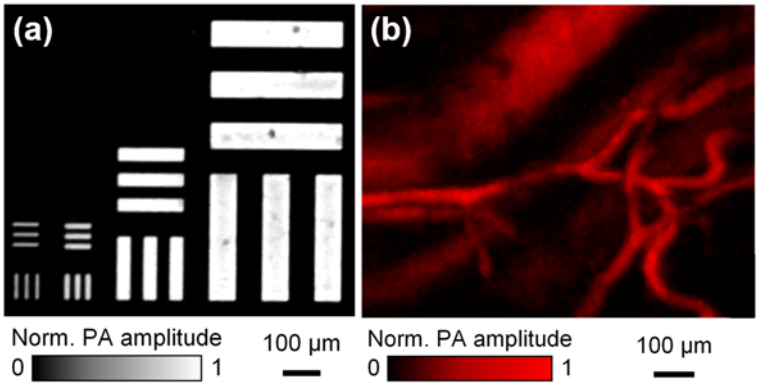

Figure 5.5 Results of the transparent-transducer–based PAM imaging. (a) MAP image of the carbon-nanotube pattern. (b) MAP image, averaged over 16 times, of an area in the mouse ear showing the vasculature by exciting the hemoglobin in RBCs.

5.4 Discussion

In this work, a thin-film optically transparent high-frequency ultrasonic transducer using ITO coated $LiNbO_3$ single-crystal was developed for PAM application. The fabricated transducer exhibited an effective electromechanical coupling coefficient k_{eff} of 0.54, a center frequency of 36.9 MHz, a –6 dB bandwidth of 33.9 %, a high sensitivity of 0.45 V peak-to-peak received voltage ($V_{p\text{-}p}$), as well as an excellent transparency of up to 90 % in the visible range. Imaging capability of the transducer for PAM was also demonstrated by successfully imaging a resolution target and mouse ear vasculature *in vivo*, with the laser beam transmitting directly through the transducer. These results will inspire further development of high-frequency ultrasonic transducers in transparent form, which will enable PAM with finer resolution. Moreover, the size of the transducer can be further reduced, making it possessing an enormous potential for developing wearable or hand-held PAM devices.

Chapter 6: Summary and outlook

In this dissertation, we have developed new technologies in the field of high-speed PAM. We applied these new technologies to translational medicine and brain functional studies, including CTC detection and therapy, and imaging cerebral hemodynamics in response to brief somatic stimulations.

In Chapter 2, we advanced previous PAM to high-speed dual-wavelength PA flow cytography for the application of CTC imaging. A concurrent on-demand laser therapy device was also developed to photothermally lyse the CTC in pinpoint manner immediately upon CTC detection. This technology is readily translatable to clinics for better cancer diagnosis, therapy efficacy assessment, and inhibiting metastasis.

In Chapter 3, we implement a novel wavelength conversion technique to address the limitation of detection sensitivity in Chapter 2. SRS was implemented to convert the pump laser to the wavelength of 658 nm. This wavelength choice resulted in an order of magnitude improvement in CNR, which facilitated reliable CTC imaging.

In Chapter 4, we further extended the SRS wavelength conversion technique to the field of high-speed functional imaging. A dual-wavelength high-speed functional PAM was developed for the studies of mouse brain hemodynamics. We successfully imaging transient micro-vascular hemodynamic changes in response to brief somatic stimulations. This technology has great promise for studies of brain functions and vascular environment.

In Chapter 5, we explored a new ultrasonic transducer technique in an effort to extend the fPAM in Chapter 4 to studies of awake animals. We sought to miniaturize the detection device by developing a thin-film optically transparent piezoelectric transducer. An ITO coated $LiNbO_3$

ultrasonic transducer was developed and its application in PAM was demonstrated with phantom and animal imaging.

There are potentially broader applications for this dissertation work with certain technological advancements. The Raman laser in Chapter 3 and Chapter 4 has a relatively large pulse energy fluctuation compared to commercial lasers. The natural solution is to implement a cooling device on the Raman crystal KGW to enable a stable thermal environment. A more stable laser can facilitate more reliable and accurate measurement of the biometric parameters.

The transparent transducer in Chapter 5 has a low detection sensitivity compared to commercial transducers. A potential solution is to find better materials for the matching layer and the electrode, as both the parylene and the ITO electrode do not match the acoustic impedance of the $LiNbO_3$.

The next step for fPAM is to integrate it to a wearable version for longitudinal studies on free-moving animals. To achieve that, both the optical scanning and ultrasonic detection devices need to be miniaturized. For the ultrasonic detection part, we explored a thin-film piezoelectric transducer, whose PAM application was demonstrated in Section 5.3. Other approaches include optical-based ultrasound detection of the PA wave using technologies such as integrated interferometer. For the optical scanning part, technologies used in laser-scanning confocally microscopy can be readily translated to wearable PAM. Other approaches include wavefront-engineering–based optical focusing.

The wavelength conversion capability of the Raman laser can also enable more applications in multi-wavelength imaging. By simultaneously employing more Stokes lines and employing pump lasers of different wavelengths, it can be applied to work with more endogenous and exogenous

contrast mechanisms, such as lipid in the near infrared region for nerve imaging, genetically encoded ion indicators, like GCaMP, for functional imaging.

References

1. Wang, L.V. & Wu, H.-i. Biomedical optics: principles and imaging. (John Wiley & Sons, 2012).
2. Wang, L.V. Tutorial on photoacoustic microscopy and computed tomography. *Selected Topics in Quantum Electronics, IEEE Journal of* **14**, 171-179 (2008).
3. Wang, L.V. & Yao, J. A practical guide to photoacoustic tomography in the life sciences. *Nature methods* **13**, 627 (2016).
4. Wang, L.V. & Hu, S. Photoacoustic tomography: in vivo imaging from organelles to organs. *Science* **335**, 1458-1462 (2012).
5. Yao, J. & Wang, L.V. Sensitivity of photoacoustic microscopy. *Photoacoustics* **2**, 87-101 (2014).
6. Wang, L., Maslov, K. & Wang, L.V. Single-cell label-free photoacoustic flowoxigraphy in vivo. *Proceedings of the National Academy of Sciences* **110**, 5759-5764 (2013).
7. Lan, B., Liu, W., Wang, Y.-c., Shi, J., Li, Y., Xu, S., Sheng, H., Zhou, Q., Zou, J. & Hoffmann, U. High-speed widefield photoacoustic microscopy of small-animal hemodynamics. *Biomedical optics express* **9**, 4689-4701 (2018).
8. Wong, T.T., Zhang, R., Hai, P., Zhang, C., Pleitez, M.A., Aft, R.L., Novack, D.V. & Wang, L.V. Fast label-free multilayered histology-like imaging of human breast cancer by photoacoustic microscopy. *Science advances* **3**, e1602168 (2017).
9. He, Y., Wang, L., Shi, J., Yao, J., Li, L., Zhang, R., Huang, C.-H., Zou, J. & Wang, L.V. In vivo label-free photoacoustic flow cytography and on-the-spot laser killing of single circulating melanoma cells. *Scientific Reports* **6**, 39616 (2016).
10. Chaffer, C.L. & Weinberg, R.A. A perspective on cancer cell metastasis. *Science* **331**, 1559-1564 (2011).
11. Steeg, P.S. Tumor metastasis: mechanistic insights and clinical challenges. *Nature medicine* **12**, 895-904 (2006).
12. Plaks, V., Koopman, C.D. & Werb, Z. Circulating tumor cells. *Science* **341**, 1186-1188 (2013).
13. Kaiser, J. Cancer's circulation problem. *Science* **327**, 1072-1074 (2010).
14. Chambers, A.F., Groom, A.C. & MacDonald, I.C. Metastasis: dissemination and growth of cancer cells in metastatic sites. *Nature Reviews Cancer* **2**, 563-572 (2002).
15. Group, U.C.S.W. United States cancer statistics: 1999–2014 incidence and mortality web-based report. *Atlanta: US Department of Health and Human Services, Centers for Disease Control and Prevention and National Cancer Institute* (2017).
16. Fidler, I.J. The pathogenesis of cancer metastasis: the'seed and soil'hypothesis revisited. *Nature Reviews Cancer* **3**, 453-459 (2003).
17. He, W., Wang, H., Hartmann, L.C., Cheng, J.-X. & Low, P.S. In vivo quantitation of rare circulating tumor cells by multiphoton intravital flow cytometry. *Proceedings of the National Academy of Sciences* **104**, 11760-11765 (2007).
18. Williams, S.C. Circulating tumor cells. *Proceedings of the National Academy of Sciences* **110**, 4861-4861 (2013).
19. Nedosekin, D.A., Verkhusha, V.V., Melerzanov, A.V., Zharov, V.P. & Galanzha, E.I. In Vivo Photoswitchable Flow Cytometry for Direct Tracking of Single Circulating Tumor Cells. *Chemistry & biology* **21**, 792-801 (2014).

20. Georgakoudi, I., Solban, N., Novak, J., Rice, W.L., Wei, X., Hasan, T. & Lin, C.P. In Vivo Flow Cytometry A New Method for Enumerating Circulating Cancer Cells. *Cancer research* **64**, 5044-5047 (2004).
21. Kienast, Y., von Baumgarten, L., Fuhrmann, M., Klinkert, W.E., Goldbrunner, R., Herms, J. & Winkler, F. Real-time imaging reveals the single steps of brain metastasis formation. *Nature medicine* **16**, 116-122 (2010).
22. Jacques, S.L. Optical properties of biological tissues: a review. *Physics in medicine and biology* **58**, R37 (2013).
23. Cheong, W.-F., Prahl, S.A. & Welch, A.J. A review of the optical properties of biological tissues. *IEEE journal of quantum electronics* **26**, 2166-2185 (1990).
24. Galanzha, E.I., Shashkov, E.V., Spring, P.M., Suen, J.Y. & Zharov, V.P. In vivo, noninvasive, label-free detection and eradication of circulating metastatic melanoma cells using two-color photoacoustic flow cytometry with a diode laser. *Cancer research* **69**, 7926-7934 (2009).
25. He, G., Xu, D., Qin, H., Yang, S. & Xing, D. In vivo cell characteristic extraction and identification by photoacoustic flow cytography. *Biomedical optics express* **6**, 3748-3756 (2015).
26. Schroeder, A., Heller, D.A., Winslow, M.M., Dahlman, J.E., Pratt, G.W., Langer, R., Jacks, T. & Anderson, D.G. Treating metastatic cancer with nanotechnology. *Nature Reviews Cancer* **12**, 39-50 (2012).
27. Streit, M. & Detmar, M. Angiogenesis, lymphangiogenesis, and melanoma metastasis. *Oncogene* **22**, 3172-3179 (2003).
28. Talmadge, J.E. & Fidler, I.J. AACR centennial series: the biology of cancer metastasis: historical perspective. *Cancer research* **70**, 5649-5669 (2010).
29. Gray-Schopfer, V., Wellbrock, C. & Marais, R. Melanoma biology and new targeted therapy. *Nature* **445**, 851-857 (2007).
30. Thomas, J.L., Lister, T.S., Royston, S.L. & Wright, P.A. Adverse effects following Q-switched ruby laser treatment of pigmented lesions. *Journal of Cosmetic and Laser Therapy* **12**, 101-105 (2010).
31. Tanzi, E.L., Lupton, J.R. & Alster, T.S. Lasers in dermatology: four decades of progress. *Journal of the American Academy of Dermatology* **49**, 1-34 (2003).
32. Anderson, R.R. & Parrish, J.A. Selective photothermolysis: precise microsurgery by selective absorption of pulsed radiation. *Science* **220**, 524-527 (1983).
33. Jacques, S.L. & McAuliffe, D.J. The melanosome: threshold temperature for explosive vaporization and internal absorption coefficient during pulsed laser irradiation. *Photochemistry and photobiology* **53**, 769-775 (1991).
34. Ara, G., Anderson, R.R., Mandel, K.G., Ottesen, M. & Oseroff, A.R. Irradiation of pigmented melanoma cells with high intensity pulsed radiation generates acoustic waves and kills cells. *Lasers in surgery and medicine* **10**, 52-59 (1990).
35. Tomayko, M.M. & Reynolds, C.P. Determination of subcutaneous tumor size in athymic (nude) mice. *Cancer chemotherapy and pharmacology* **24**, 148-154 (1989).
36. Maslov, K., Stoica, G. & Wang, L.V. In vivo dark-field reflection-mode photoacoustic microscopy. *Optics letters* **30**, 625-627 (2005).
37. Zhang, H.F., Maslov, K., Stoica, G. & Wang, L.V. Functional photoacoustic microscopy for high-resolution and noninvasive in vivo imaging. *Nature biotechnology* **24**, 848-851 (2006).

38. Chen, W.R., Carubelli, R., Liu, H. & Nordquist, R.E. Laser immunotherapy. *Molecular biotechnology* **25**, 37-43 (2003).
39. Massagué, J. & Obenauf, A.C. Metastatic colonization by circulating tumour cells. *Nature* **529**, 298-306 (2016).
40. Cristofanilli, M., Budd, G.T., Ellis, M.J., Stopeck, A., Matera, J., Miller, M.C., Reuben, J.M., Doyle, G.V., Allard, W.J. & Terstappen, L.W. Circulating tumor cells, disease progression, and survival in metastatic breast cancer. *New England Journal of Medicine* **351**, 781-791 (2004).
41. Cristofanilli, M., Hayes, D.F., Budd, G.T., Ellis, M.J., Stopeck, A., Reuben, J.M., Doyle, G.V., Matera, J., Allard, W.J. & Miller, M.C. Circulating tumor cells: a novel prognostic factor for newly diagnosed metastatic breast cancer. *Journal of Clinical Oncology* **23**, 1420-1430 (2005).
42. Balic, M., Williams, A., Lin, H., Datar, R. & Cote, R.J. Circulating tumor cells: from bench to bedside. *Annual review of medicine* **64**, 31-44 (2013).
43. Attard, G. & de Bono, J.S. Utilizing circulating tumor cells: challenges and pitfalls. *Current opinion in genetics & development* **21**, 50-58 (2011).
44. Karakousis, G., Yang, R. & Xu, X. Circulating melanoma cells as a predictive biomarker. *Journal of Investigative Dermatology* **133**, 1460-1462 (2013).
45. Wang, X., Qian, X., Beitler, J.J., Chen, Z.G., Khuri, F.R., Lewis, M.M., Shin, H.J.C., Nie, S. & Shin, D.M. Detection of circulating tumor cells in human peripheral blood using surface-enhanced Raman scattering nanoparticles. *Cancer research* **71**, 1526-1532 (2011).
46. Cummins, D.L., Cummins, J.M., Pantle, H., Silverman, M.A., Leonard, A.L. & Chanmugam, A. Cutaneous malignant melanoma. *Mayo Clinic proceedings* **81**, 500-507 (2006).
47. Xu, L., Alam, S., Kang, Q., Shepherd, D. & Richardson, D. Raman-shifted wavelength-selectable pulsed fiber laser with high repetition rate and high pulse energy in the visible. *Optics express* **25**, 351-356 (2017).
48. Allen, T., Berendt, M., Spurrell, J., Alam, S., Zhang, E., Richardson, D. & Beard, P. in Photons Plus Ultrasound: Imaging and Sensing 2016, Vol. 9708 97080W (International Society for Optics and Photonics, 2016).
49. Mildren, R., Convery, M., Pask, H., Piper, J. & Mckay, T. Efficient, all-solid-state, Raman laser in the yellow, orange and red. *Optics express* **12**, 785-790 (2004).
50. Islam, M.N. Raman amplifiers for telecommunications 1: Physical principles, Vol. 90. (Springer, 2007).
51. Liao, L.-D., Lin, C.-T., Shih, Y.-Y.I., Duong, T.Q., Lai, H.-Y., Wang, P.-H., Wu, R., Tsang, S., Chang, J.-Y. & Li, M.-L. Transcranial imaging of functional cerebral hemodynamic changes in single blood vessels using in vivo photoacoustic microscopy. *Journal of Cerebral Blood Flow & Metabolism* **32**, 938-951 (2012).
52. Hu, X. & Yacoub, E. The story of the initial dip in fMRI. *Neuroimage* **62**, 1103-1108 (2012).
53. Menon, R.S., Ogawa, S., Hu, X., Strupp, J.P., Anderson, P. & Uğurbil, K. BOLD based functional MRI at 4 Tesla includes a capillary bed contribution: echo-planar imaging correlates with previous optical imaging using intrinsic signals. *Magnetic resonance in medicine* **33**, 453-459 (1995).

54. Kim, D.-S., Duong, T.Q. & Kim, S.-G. High-resolution mapping of iso-orientation columns by fMRI. *Nature neuroscience* **3**, 164 (2000).
55. Logothetis, N.K. What we can do and what we cannot do with fMRI. *Nature* **453**, 869 (2008).
56. Raichle, M.E. Behind the scenes of functional brain imaging: a historical and physiological perspective. *Proceedings of the National Academy of Sciences* **95**, 765-772 (1998).
57. Vanzetta, I. & Grinvald, A. Coupling between neuronal activity and microcirculation: implications for functional brain imaging. *HFSP journal* **2**, 79-98 (2008).
58. Huettel, S.A., Song, A.W. & McCarthy, G. Functional magnetic resonance imaging, Vol. 1. (Sinauer Associates Sunderland, MA, 2004).
59. Mayhew, J., Johnston, D., Berwick, J., Jones, M., Coffey, P. & Zheng, Y. Spectroscopic analysis of neural activity in brain: increased oxygen consumption following activation of barrel cortex. *Neuroimage* **12**, 664-675 (2000).
60. Sirotin, Y.B., Hillman, E.M., Bordier, C. & Das, A. Spatiotemporal precision and hemodynamic mechanism of optical point spreads in alert primates. *Proceedings of the National Academy of Sciences* **106**, 18390-18395 (2009).
61. Hong, K.-S. & Zafar, A. Existence of initial dip for BCI: an illusion or reality. *Frontiers in neurorobotics* **12** (2018).
62. Uludağ, K. To dip or not to dip: reconciling optical imaging and fMRI data. *Proceedings of the National Academy of Sciences* **107**, E23-E23 (2010).
63. Devor, A., Dunn, A.K., Andermann, M.L., Ulbert, I., Boas, D.A. & Dale, A.M. Coupling of total hemoglobin concentration, oxygenation, and neural activity in rat somatosensory cortex. *Neuron* **39**, 353-359 (2003).
64. Buxton, R.B. The elusive initial dip. *Neuroimage* **13**, 953-958 (2001).
65. Goense, J., Merkle, H. & Logothetis, N.K. High-resolution fMRI reveals laminar differences in neurovascular coupling between positive and negative BOLD responses. *Neuron* **76**, 629-639 (2012).
66. Tian, P., Teng, I.C., May, L.D., Kurz, R., Lu, K., Scadeng, M., Hillman, E.M., De Crespigny, A.J., D'Arceuil, H.E. & Mandeville, J.B. Cortical depth-specific microvascular dilation underlies laminar differences in blood oxygenation level-dependent functional MRI signal. *Proceedings of the National Academy of Sciences* **107**, 15246-15251 (2010).
67. Devor, A., Sakadžić, S., Saisan, P.A., Yaseen, M.A., Roussakis, E., Srinivasan, V.J., Vinogradov, S.A., Rosen, B.R., Buxton, R.B. & Dale, A.M. "Overshoot" of O2 is required to maintain baseline tissue oxygenation at locations distal to blood vessels. *Journal of Neuroscience* **31**, 13676-13681 (2011).
68. Frostig, R.D., Lieke, E.E., Ts'o, D.Y. & Grinvald, A. Cortical functional architecture and local coupling between neuronal activity and the microcirculation revealed by in vivo high-resolution optical imaging of intrinsic signals. *Proceedings of the National Academy of Sciences* **87**, 6082-6086 (1990).
69. Ma, Y., Shaik, M.A., Kim, S.H., Kozberg, M.G., Thibodeaux, D.N., Zhao, H.T., Yu, H. & Hillman, E.M. Wide-field optical mapping of neural activity and brain haemodynamics: considerations and novel approaches. *Philosophical Transactions of the Royal Society B: Biological Sciences* **371**, 20150360 (2016).

70. Hillman, E.M., Devor, A., Bouchard, M.B., Dunn, A.K., Krauss, G., Skoch, J., Bacskai, B.J., Dale, A.M. & Boas, D.A. Depth-resolved optical imaging and microscopy of vascular compartment dynamics during somatosensory stimulation. *Neuroimage* **35**, 89-104 (2007).
71. Yao, J., Wang, L., Yang, J.-M., Maslov, K.I., Wong, T.T., Li, L., Huang, C.-H., Zou, J. & Wang, L.V. High-speed label-free functional photoacoustic microscopy of mouse brain in action. *Nature methods* **12**, 407 (2015).
72. Shung, K.K. & Thieme, G.A. Ultrasonic scattering in biological tissues. (CRC press, 1992).
73. Zhang, H.F., Maslov, K., Sivaramakrishnan, M., Stoica, G. & Wang, L.V. Imaging of hemoglobin oxygen saturation variations in single vessels in vivo using photoacoustic microscopy. *Applied physics letters* **90**, 053901 (2007).
74. de La Cruz-May, L., Alvarez-Chavez, J.A., Mejía, E., Flores-Gil, A., Mendez-Martinez, F. & Wabnitz, S. Raman threshold for nth-order cascade Raman amplification. *Optical Fiber Technology* **17**, 214-217 (2011).
75. Urey, H. Torsional MEMS scanner design for high-resolution scanning display systems, Vol. 4773. (SPIE, 2002).
76. Hu, S., Maslov, K. & Wang, L.V. Second-generation optical-resolution photoacoustic microscopy with improved sensitivity and speed. *Optics letters* **36**, 1134-1136 (2011).
77. Zhang, C., Maslov, K.I., Yao, J. & Wang, L.V. In vivo photoacoustic microscopy with 7.6-μm axial resolution using a commercial 125-MHz ultrasonic transducer. *Journal of biomedical optics* **17**, 116016 (2012).
78. Jerman, T., Pernuš, F., Likar, B. & Špiclin, Ž. Enhancement of vascular structures in 3D and 2D angiographic images. *IEEE transactions on medical imaging* **35**, 2107-2118 (2016).
79. Jones, M., Berwick, J., Johnston, D. & Mayhew, J. Concurrent optical imaging spectroscopy and laser-Doppler flowmetry: the relationship between blood flow, oxygenation, and volume in rodent barrel cortex. *Neuroimage* **13**, 1002-1015 (2001).
80. MacDougall, J. & McCabe, M. Diffusion coefficient of oxygen through tissues. *Nature* **215**, 1173 (1967).
81. Klitzman, B., Popel, A.S. & Duling, B.R. Oxygen transport in resting and contracting hamster cremaster muscles: experimental and theoretical microvascular studies. *Microvascular research* **25**, 108-131 (1983).
82. Buma, T., Wilkinson, B.C. & Sheehan, T.C. Near-infrared spectroscopic photoacoustic microscopy using a multi-color fiber laser source. *Biomedical optics express* **6**, 2819-2829 (2015).
83. Wang, P., Ma, T., Slipchenko, M.N., Liang, S., Hui, J., Shung, K.K., Roy, S., Sturek, M., Zhou, Q. & Chen, Z. High-speed intravascular photoacoustic imaging of lipid-laden atherosclerotic plaque enabled by a 2-kHz barium nitrite raman laser. *Scientific reports* **4**, 6889 (2014).
84. Liang, Y., Jin, L., Guan, B.-O. & Wang, L. 2 MHz multi-wavelength pulsed laser for functional photoacoustic microscopy. *Optics letters* **42**, 1452-1455 (2017).
85. Koeplinger, D., Liu, M. & Buma, T. in Ultrasonics Symposium (IUS), 2011 IEEE International 296-299 (IEEE, 2011).
86. Qiu, M., Ramani, R., Swetye, M., Rajeevan, N. & Constable, R.T. Anesthetic effects on regional CBF, BOLD, and the coupling between task-induced changes in CBF and

BOLD: An fMRI study in normal human subjects. *Magnetic Resonance in Medicine: An Official Journal of the International Society for Magnetic Resonance in Medicine* **60**, 987-996 (2008).
87. Martin, C., Martindale, J., Berwick, J. & Mayhew, J. Investigating neural–hemodynamic coupling and the hemodynamic response function in the awake rat. *Neuroimage* **32**, 33-48 (2006).
88. Ntziachristos, V. Going deeper than microscopy: the optical imaging frontier in biology. *Nature methods* **7**, 603 (2010).
89. Maslov, K., Zhang, H.F., Hu, S. & Wang, L.V. Optical-resolution photoacoustic microscopy for in vivo imaging of single capillaries. *Optics letters* **33**, 929-931 (2008).
90. Shi, J., Wong, T.T.W., He, Y., Li, L., Zhang, R., Yung, C.S., Hwang, J., Maslov, K. & Wang, L.V. High-resolution, high-contrast mid-infrared imaging of fresh biological samples with ultraviolet-localized photoacoustic microscopy. *Nature Photonics* **13**, 609-615 (2019).
91. Zhang, C., Maslov, K.I., Hu, S., Wang, L.V., Chen, R., Zhou, Q. & Shung, K.K. Reflection-mode submicron-resolution in vivo photoacoustic microscopy. *Journal of biomedical optics* **17**, 020501 (2012).
92. Wong, T.T., Zhang, R., Zhang, C., Hsu, H.-C., Maslov, K.I., Wang, L., Shi, J., Chen, R., Shung, K.K. & Zhou, Q. Label-free automated three-dimensional imaging of whole organs by microtomy-assisted photoacoustic microscopy. *Nature communications* **8**, 1386 (2017).
93. Zhang, E. & Beard, P. Broadband ultrasound field mapping system using a wavelength tuned, optically scanned focused laser beam to address a Fabry Perot polymer film sensor. *ieee transactions on ultrasonics, ferroelectrics, and frequency control* **53**, 1330-1338 (2006).
94. Ansari, R., Zhang, E., Desjardins, A. & Beard, P. in Photons Plus Ultrasound: Imaging and Sensing 2017, Vol. 10064 100641W (International Society for Optics and Photonics, 2017).
95. Chen, S.-L., Guo, L.J. & Wang, X. All-optical photoacoustic microscopy. *Photoacoustics* **3**, 143-150 (2015).
96. Niederhauser, J., Jaeger, M., Hejazi, M., Keppner, H. & Frenz, M. Transparent ITO coated PVDF transducer for optoacoustic depth profiling. *Optics communications* **253**, 401-406 (2005).
97. Blumenröther, E., Melchert, O., Kanngießer, J., Wollweber, M. & Roth, B. Single Transparent Piezoelectric Detector for Optoacoustic Sensing—Design and Signal Processing. *Sensors* **19**, 2195 (2019).
98. Li, Z., Ilkhechi, A.K. & Zemp, R. Transparent capacitive micromachined ultrasonic transducers (CMUTs) for photoacoustic applications. *Optics express* **27**, 13204-13218 (2019).
99. Chua, S.-J. & Li, B. Optical switches: materials and design. (Elsevier, 2010).
100. Cannata, J.M., Ritter, T.A., Chen, W.-H., Silverman, R.H. & Shung, K.K. Design of efficient, broadband single-element (20-80 MHz) ultrasonic transducers for medical imaging applications. *IEEE transactions on ultrasonics, ferroelectrics, and frequency control* **50**, 1548-1557 (2003).

101. Brodie, G.W., Qiu, Y., Cochran, S., Spalding, G.C. & Macdonald, M.P. Optically transparent piezoelectric transducer for ultrasonic particle manipulation. *IEEE transactions on ultrasonics, ferroelectrics, and frequency control* **61**, 389-391 (2014).
102. Dangi, A., Agrawal, S. & Kothapalli, S.-R. Lithium niobate-based transparent ultrasound transducers for photoacoustic imaging. *Optics Letters* **44**, 5326-5329 (2019).
103. Meeker, T. Publication and proposed revision of ANSI/IEEE standard 176-1987. *IEEE Transactions on Ultrasonics Ferroelectrics and Frequency Control* **43**, 717-772 (1996).
104. Chen, R., Jiang, L., Zhang, T., Matsuoka, T., Yamazaki, M., Qian, X., Lu, G., Safari, A., Zhu, J. & Shung, K.K. Eco-Friendly Highly Sensitive Transducers Based on a New KNN–NTK–FM Lead-Free Piezoelectric Ceramic for High-Frequency Biomedical Ultrasonic Imaging Applications. *IEEE Transactions on Biomedical Engineering* **66**, 1580-1587 (2018).